RSC Advances

PAPER

View Article Online
View Journal | View Issue

Cite this: *RSC Adv.*, 2026, **16**, 19524

Ferulic and *p*-coumaric acid derivatives as dual EGFR-VEGFR2 inhibitors: design, semi-synthesis, and biological investigations

Ranza Elrayess, †*[ab] Mohamed S. Nafie, †[cd] Safwat A. Ahmed,[e] Yosra K. Alkazzaz,[f] Khaled M. Darwish, [gh] Heba N. Gad El-Hak[i] and Enas E. Eltamany *[e]

Since there is a great deal of interest in the examination of the potential role of herbal and complementary medicines in the treatment of different types of cancer, we report here the semi-synthesis of novel derivatives of the naturally occurring *P*-CA and FA as dual EGFR/VEGFR2 inhibitors and investigate their cytotoxicity through *in vitro* and *in vivo* studies, shedding light on their potential and mechanism of action. The synthesized compounds were evaluated for their cytotoxicity against MCF-7, HepG-2, A549 cell lines, and WISH normal cells. Compounds **3d**, **3f**, and **3h** showed potent cytotoxicity against MCF-7 with IC_{50} values of 1.16, 1.04, and 1.1 μM, respectively, compared to Sorafenib (IC_{50} = 3.04 μM). Interestingly, compound **3f**, the most active compound, exhibited potent EGFR and VEGFR2 inhibition with an IC_{50} value of 75.4 nM and 36.2 nM, respectively, compared to Sorafenib with an EGFR and VEGFR2 inhibition IC_{50} values of 69.8 nM and 30.1 nM. Additionally, compound **3f** dramatically induced apoptotic cell death in MCF-7 cells, increasing the death rate by 32.9% compared to 0.95% in the untreated control. Furthermore, compound **3f** treatment significantly increased the cell population at the G1-phase by 79.6% compared to control 53.3%, while cells in S and G2/M phases decreased and caused cell death in MCF-7 cells, stopping their growth in the G1 phase. *In vivo* studies revealed that compound **3f** and Sorafenib decreased the mass of solid tumor to 132 mg and 116 mg, respectively. Accordingly, the tumor volume was reduced from 319 mm^3 in the SEC-bearing model to 134 mm^3 and 119.6 mm^3, respectively. Hence, both treatments inhibited tumor proliferation by 57.9% and 62.5%, respectively. Ultimately, a histological evaluation was conducted to assess compound **3f**'s efficacy and safety. Finally, molecular docking revealed the bias of both EGFR and VEGFR2 pockets towards compound **3f** compared to other synthesized compounds. The docking scores obtained for **3f** against EGFR and VEGFR2 indicated comparable binding profiles at ΔG scores −9.48 and −10.12 kcal mol^{-1}, respectively, exhibiting a quite higher binding affinity than the other analogs. The results revealed that compound **3f** had promising structural and functional properties, making it a promising candidate for further research into the design and development of more active analogs.

Received 10th February 2026
Accepted 6th April 2026

DOI: 10.1039/d6ra01213b

rsc.li/rsc-advances

1 Introduction

In drug discovery research, natural products are a significant source of novel lead compounds. Numerous medications currently in use as therapeutic agents were created using natural sources, with plants playing a particularly significant role.[1] Additionally, organic compounds derived from natural sources have been employed in the past and continue to be used to treat a variety of diseases; these compounds are utilized in their natural state (as pure drugs or phytomedicine) and as lead molecules for the development of synthetic and semi-synthetic analogues with enhanced druggability.[2–4]

[a]*Pharmaceutical Organic Chemistry Department, Faculty of Pharmacy, Suez Canal University, Ismailia 41522, Egypt. E-mail: Ranza.el-rayes@pharm.suez.edu.eg*
[b]*Pharmaceutical Organic Chemistry Department, College of Pharmacy, Al-Ayen Iraqi University, An Nasiriyah, 64001, Iraq*
[c]*Department of Chemistry, College of Sciences, University of Sharjah, Sharjah, 27272, United Arab Emirates*
[d]*Department of Chemistry, Faculty of Science, Suez Canal University, Ismailia 41522, Egypt*
[e]*Department of Pharmacognosy, Faculty of Pharmacy, Suez Canal University, Ismailia 41522, Egypt. E-mail: enas_mostafa@pharm.suez.edu.eg*
[f]*Institute of Biotechnology for Postgraduate Studies and Research, Suez Canal University, Ismailia, 41522, Egypt*
[g]*Department of Medicinal Chemistry, Faculty of Pharmacy, Suez Canal University, Ismailia, Egypt*
[h]*Department of Medicinal Chemistry, Faculty of Pharmacy, Galala University, New Galala 43713, Egypt*
[i]*Department of Zoology, Faculty of Science, Suez Canal University, Ismailia 41522, Egypt*
† Ranza Elrayess and Mohamed S. Nafie contributed equally to this study.

Among the most prevalent dietary pharmacologically active natural metabolites are the hydroxycinnamates, such as the *p*-coumaric and ferulic acids. The *p*-coumaric acid (*p*-CA) has a well-proven wide range of therapeutic capabilities including antitumor, anti-inflammatory, antioxidant activities,[5,6] as well as chemoprotective, cardioprotective, and neuroprotective properties.[7,8] Its capacity to regulate a variety of metabolic pathways, such as apoptosis, necrosis, angiogenesis, and inflammation, makes it a potent anticancer drug.[9] However, because of its unfavored bioavailability and biocompatibility, *p*-CA's use as an anticancer medication has been exceptionally restricted, triggering scientists towards compound derivatization. The majority of *p*-CA derivatives and compounds with a phenethyl moiety showed prominent activities were adding a phenethyl moiety with a *p*-coumaroyl group boosted the *p*-CA's anticancer potential.[10] The ester phenethyl *p*-coumarate **I** and amide *N*-phenethyl-*p*-coumaramide **II** (Fig. 1) yielded IC_{50} values of 1.0 and 5.89 μg mL^{-1}, respectively, on P388 leukemia murine cells.[10] According to a 2023 study by Joana *et al.*,[11] esterification of *p*-CA (**III** and **IV**) enhanced the regulation of human and murine melanoma cell growth and may be a strategy for creating new anticancer drugs.[11] Targeting the breast cancer cell line, reports highlighted relevant antitumor activity of *p*-CA towards the MCF-7 cancerous cell line where apoptosis induction, suppression of the RAS genes, and activation of Janus kinase/p38/MAPK, where relevant with the natural molecule.[12,13] Several semi-synthetic *p*-CA analogs of coupled *p*-CA molecule with amino acid scaffolds **V** (*e.g.* threonine, lysine, or phenylalanine) yielded relevant selectivity indices (up to 5.1) and micromolar range IC_{50} (≈39 μM).[14]

Ferulic acid (FA) has well-known therapeutic endeavors such as anti-inflammatory,[15,16] antioxidant,[17] and antitumor properties.[18–21] In 2012, Li *et al.* used a high-throughput screening (HTS) method to evaluate the anticancer properties of alkyl esters and NO-donors of ferulic acid (FA) and caffeic acid (CA), and they reported the structure–activity connections. Phenylsulfonyl furoxan nitrates **VI**, **VII**, and **VIII** (Fig. 1) exhibited powerful anticancer activity against every human cancer cell in the NO-donor series. All of them had IC_{50} values below 10 μM.[19] Ferulic acid fructo-oligosaccharide (FA FOS) conjugate was synthesized by Eldin *et al.* in 2023. The group treated with FA FOS had 60.83% fewer tumor lesions than the

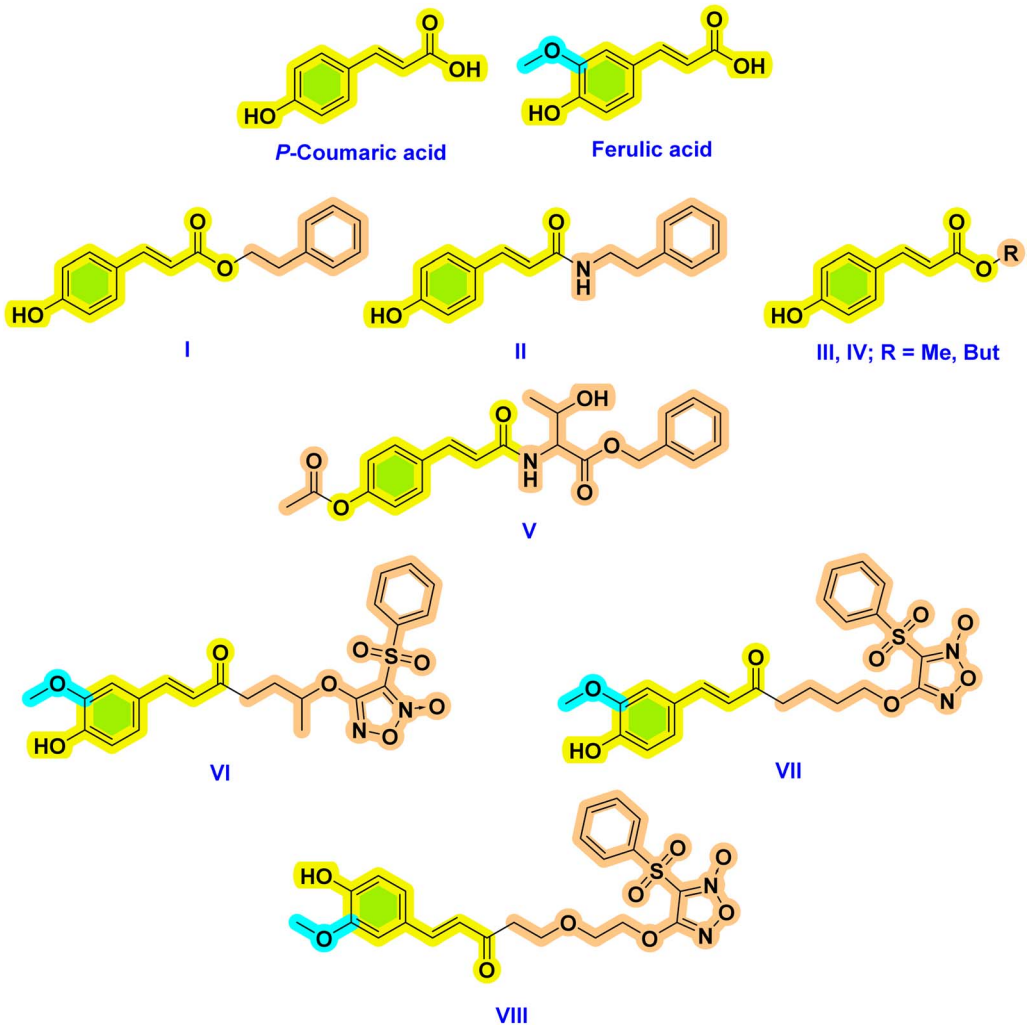

Fig. 1 Structure of reported *p*-coumaric and ferulic acid derivatives with anticancer activities.

control group.[22] Suggested molecular signaling pathways were through p38/MAPK/ERK, PI3K/AKT, NF-κB, and AKT/mTOR signaling lineages.[23]

As highlighted above, molecular aspects of *p*-CA anticancer activity have been highlighted to target several kinases signaling pathways. Among the most interesting cancer-associated kinase families are the tyrosine kinases which have garnered a lot of attention as possible targets for cancer treatments because of their crucial roles in cellular signaling cascades.[24] Currently, more than 70 druggable small-molecule inhibitors of the protein kinases have been approved by the US-FDA, while another additional 16 kinase inhibitors were approved by other regulatory bodies. One member of the superfamily of tyrosine kinases is the epidermal growth factor receptor (EGFR), which regulates a number of biological processes, including cell division, growth, survival, proliferation, and apoptosis. Increased cellular growth, aggression, and invasiveness traits have been linked to EGFR overexpression in cancer cells, which has also been linked to triggered downstream signaling pathways. As a result, EGFR has emerged as a key target for the treatment of several malignancies, such as non-small cell lung, breast, colon, and prostate cancers.[25] The type V receptor tyrosine kinase, vascular endothelial growth factor receptor 2 (VEGFR2), is predominantly expressed in vascular endothelial cells.[26] It regulates angiogenesis and plays a vital role in both cancer development and normal human development.[27] VEGFR2 expressions in carcinoma cells have been documented in numerous studies, particularly in colorectal, non-small cell lung, urothelial, and mammary carcinomas. Diffuse large B-cell lymphoma and malignant melanoma have also been linked to tumor cell expression.[26] As a result, blocking VEGFR-2 has been established as a treatment strategy for cancer.

The two kinase biotargets, EGFR and VEGFR2, share a common signaling pathways, where EGFR blockage can lead to a reduction in VEGF production that finally suppresses angiogenesis. However, this kind of suppression can paradoxically drive a compensatory overexpression of VEGFR2 within the later therapeutic stages which would contribute to the development of cancer resistance in a phenomenon further being demonstrated with long-term administration of EGFR inhibitors.[28,29] As a result, simultaneous inhibition of VEGFR2, alongside EGFR, has emerged as a promising strategy to synergistically enhance therapeutic outcomes and delay/prevent the emergence of cancer resistance. Clinical evidence highlighting the therapeutic combination of Erlotinib (EGFR inhibitor) with Foretinib (Mesenchymal Epithelial Transition (MET)/VEGFR2 inhibitor) postulated clinical responses in patients with locally advanced or metastatic non-small cell lung cancer (NSCLC) at phase I/II clinical trials (NCT01068587).

Correlating the natural molecules towards the two kinases, it has been reported that both FA and *P*-CA can down-regulate EGFR expression.[30] Apart from its anti-proliferative action, *P*-CA has been demonstrated to inhibit the expression of the EGFR gene in HCT-15 cells. Furthermore, in the colon tissue of rats treated with DMH, *P*-CA co-administration reduced the expression of angiogenic proteins (VEGF, PDGF, and bFGF).[31] In addition to blocking the AKT and ERK signaling pathways, which are known to be essential for angiogenesis, *P*-CA also suppressed the tube formation, migration, and sprouting of endothelial cells in rat aortic rings. It was also able to down-regulate the mRNA expression levels of the two main angiogenic factors, vascular endothelial growth factor and basic fibroblast growth factor. Collectively, these results show that FA and *P*-CA acid have strong anticancer effects due to their ability to inhibit EGFR and VEGFR2.[32,33] Nonetheless, the physiochemical properties of these parent molecules still represent a significant barrier towards their sole applications. In these regards, we here in our study report the semi-synthetic derivatization of *p*-CA and FA to furnish novel small molecule analogs with improved properties, as well as capable of dual targeting EGFR/VEGFR2 for inhibition. The anti-proliferative activity against cancer was thoroughly investigated through *in vitro* and *in vivo* studies as well as computational approach for shedding the light on their mechanistic activities down to their molecular levels.

2 Rational

Natural phenolics may be modified semi-synthetically to increase bioactivity. Their pharmacological potential may be enhanced by adding functional groups or other structural modifications that increase solubility, stability, and their ability to interact with biological targets. Phenolic hydroxyl groups can be esterified, alkylated, or glycosylated to create molecules with increased activity and selectivity.[1] These modifications enhance the efficacy of treatment and contribute to the comprehension of the structure–activity relationship (SAR) of phenolic compounds. Their binding affinity to enzymes, receptors, or biological pathways may be increased by strategic functionalization, offering new leads for drug discovery.[34] On the other hand, a class of nitrogenous chemicals known as hydrazides, hydrazones, and acyl hydrazones has been the subject of much research and has been used in a variety of therapeutically intriguing anticancer drugs.[35]

One of the most promising approaches to developing novel candidates that could increase affinity and efficacy while overcoming cross-resistance and/or adverse effects in comparison to the parent medications is hybridization.[25] Given the significance of hybrid molecules in the management of many cancer kinds and routes.[36–38] Herein, we introduce the design of novel FA and *P*-CA–hydrazone hybrids (Fig. 2) that combine FA or *p*-CA and hydrazone into a single compact structure, which can target cancer-associated biotargets. We further incorporated within our designed compounds the key pharmacophoric features of both EGFR/VEGFR2 kinases. Typically, such dual inhibitors incorporate structural elements including hinge-binding moieties, aryl hydrophobic scaffolds, and hydrogen bond donors/acceptors that are capable of interacting with the target's DFG motif, which is crucially involved in kinase activation. Aligned with the above structural requirements, the hydrazide–hydrazone moiety possesses polar capabilities (hydrogen bond acceptors/donors) to engage with the amino acids at the kinase hinge region. The presence of a central aromatic core would be relevant for mediating hydrophobic contacts with the kinases' central sub-pocket. The other

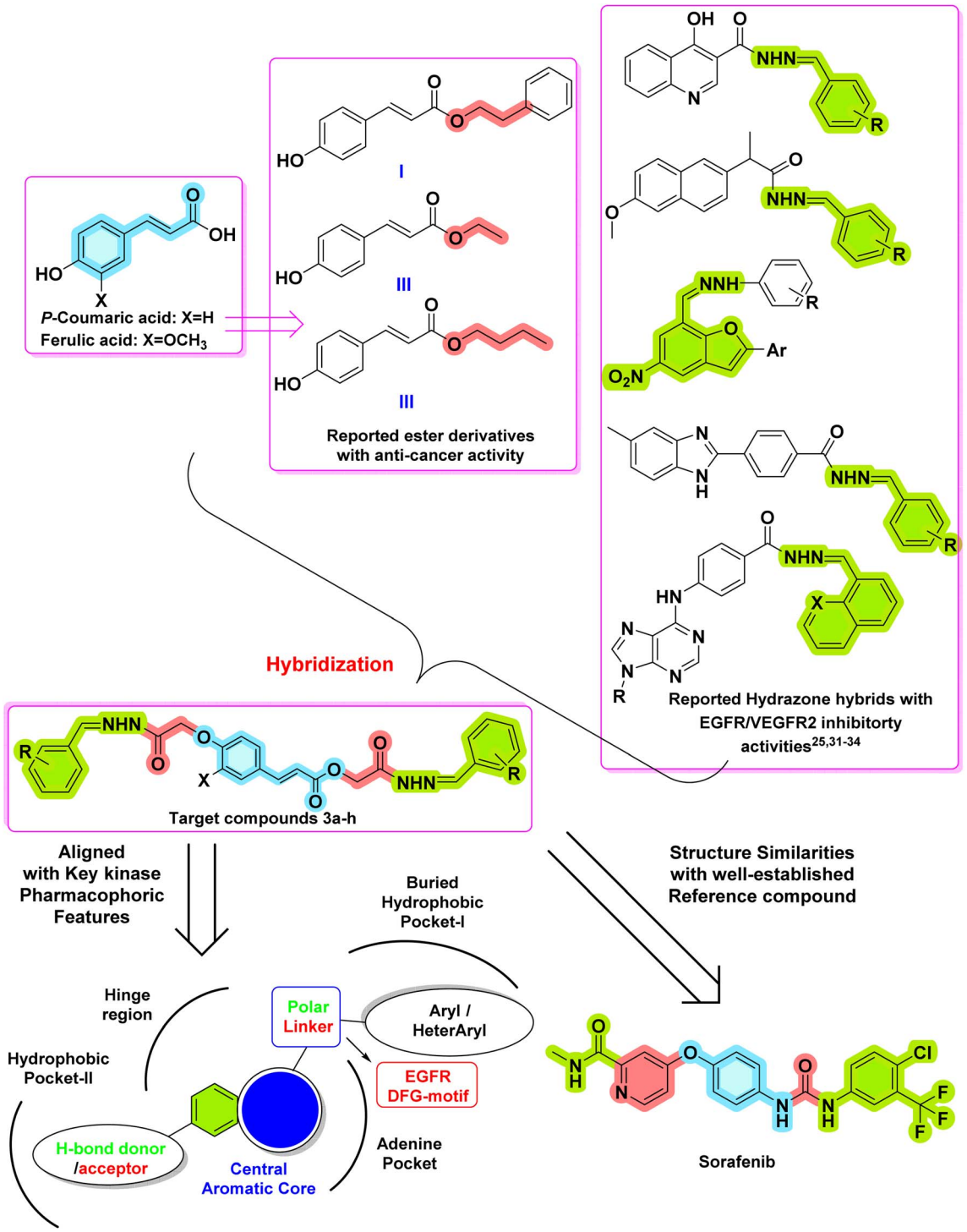

Fig. 2 Design of target compounds 3a–h.

hydrazide–hydrazone moiety on the other side of the compounds we designed to mediate relevant polar interactions at the DFG-motif which is reported important for potent kinase inhibitors.[39] Finally, the aromatic terminal rings were incorporated to satisfy the double hydrophobic site on both sides of the ATP's adenine site. It is worth mentioning that our synthesized analogs also retain the key pharmacophoric characteristics of Sorafenib (Fig. 2), as well-established multi-kinase inhibitor exerting its anticancer activity through hampering several signaling pathways, most notably VEGFR2-mediated angiogenesis, while also suppressing the tumor cell proliferation within EGFR-related signaling pathways. For the SAR analysis of these compounds, the produced compounds have varied

replacements with electron-releasing/electron-withdrawing groups at the terminal aromatic moieties.

3 Materials and methods

3.1 Chemistry

Scheme 1 depicted the synthetic approach for the desired compounds, which was carried out following the reported procedures.[40–42] The synthetic procedures are included in the SI. Instruments, chemicals, and reagents used in preparing and confirming target compounds are presented in the SI.

3.1.1 2-(2-((*E*)-Benzylidene) hydrazinyl)-2-oxoethyl (*E*)-3-(4-(2-(2-((*E*)-benzylidene) hydrazinyl)-2-oxoethoxy) phenyl) acrylate (3a). White; yield 92%; M.p.; 168–170 °C; IR (cm^{-1}): 3256 (NH), 1684 (N=C), 1667 (C=O), 1248 (C–O–C). EI-MS (*m*/*z*, %): 484 (M^+); ^{1}H NMR (400 MHz, DMSO-d_6): δ 11.63 (s, 1H, N**H**), 8.34 (s, 1H, C**H**=N), 8.03 (s, 1H, C**H**=N), 7.71–7.65 (m, 8H, Ar–**H**), 7.62 (d, J = 16 Hz, 1H, C**H**=CH), 7.43–6.97 (m, 6H, Ar–**H**), 6.48 (d, J = 16 Hz, 1H, CH=C**H**), 5.21 (s, 2H, COO–**CH$_2$**), 4.74 (s, 1H, N**H**), 3.70 (s, 2H, O–**CH$_2$**); ^{13}C NMR (101 MHz, DMSO-d_6) δ 168.71 (2C), 166.91, 160.14, 144.27 (2C), 143.95, 133.94, 130.01 (2C), 128.81 (4C), 128.78 (4C), 127.14 (2C), 126.95 (2C), 115.56 (2C), 114.95, 66.43, 64.80. Anal. calcd. for $C_{27}H_{24}N_4O_5$: C, 66.93; H, 4.99; N, 11.56; O, 16.51. Found: C, 67.19; H, 5.07; N, 11.78.

3.1.2 2-(2-((*E*)-3-Nitrobenzylidene)hydrazinyl)-2-oxoethyl(-*E*)-3-(4-(2-(2-((*E*)-3-nitrobenzylidene)hydrazinyl)-2-oxoethoxy) phenyl)acrylate (3b). White; yield 74%; M.p.; 198–200 °C; IR (cm^{-1}): 3540 (NH), 1664 (N=C), 1619 (C=O), 1522 (NO_2 Asym), 1399 (NO_2 Sym), 1245 (C–O–C). EI-MS (*m*/*z*, %): 574 (M^+); ^{1}H NMR (400 MHz, DMSO-d_6): δ 11.88 (s, 1H, N**H**), 8.52 (s, 1H, C**H**=N), 8.46 (s, 1H, C**H**=N), 8.28–7.66 (m, 9H, Ar–**H**), 7.63 (d, J = 16 Hz, 1H, C**H**=CH), 7.06–6.98 (m, 3H, Ar–**H**), 6.50 (d, J = 16 Hz, 1H, CH=C**H**), 5.28 (s, 2H, COO–**CH$_2$**), 4.78 (s, 1H, N**H**), 3.72 (s, 2H, O–**CH$_2$**); ^{13}C NMR (101 MHz, DMSO-d_6) δ 169.54 (2C), 167.41, 160.58, 148.73 (2C), 146.12, 144.75 (2C), 133.41 (2C), 130.85 (2C), 130.59 (2C), 130.49 (2C), 127.35, 124.69 (2C), 121.75 (2C), 116.06, 115.45 (2C), 66.82, 65.30. Anal. calcd. for: $C_{27}H_{22}N_6O_9$: C, 56.45; H, 3.86; N, 14.63; O, 25.06. Found: C, 56.71; H, 3.98; N, 14.89.

3.1.3 2-(2-((*E*)-3-Methoxybenzylidene)hydrazinyl)-2-oxo-ethyl(*E*)-3-(4-(2-(2-((*E*)-3-methoxybenzylidene)hydrazinyl)-2-oxoethoxy)phenyl)acrylate (3c). Piege; yield 72%; M.p.; 162–164 °C; IR (cm^{-1}): 3484 (NH), 1668 (N=C), 1631 (C=O), 1244 (C–O–C). EI-MS (*m*/*z*, %): 544 (M^+); ^{1}H NMR (400 MHz, DMSO-d_6): δ 11.66 (s, 1H, N**H**), 8.33 (s, 1H, C**H**=N), 8.01 (s, 1H, C**H**=N), 7.71–7.67 (m, 3H, Ar–**H**), 7.63 (d, J = 16 Hz, 1H, C**H**=CH), 7.38–6.98 (m, 9H, Ar–**H**), 6.48 (d, J = 16 Hz, 1H, CH=C**H**), 5.23 (s, 2H, COO–**CH$_2$**), 4.76 (s, 1H, N**H**), 3.80 (s, 6H, 2× OC**H$_3$**), 3.72 (s, 2H, O–**CH$_2$**). ^{13}C NMR (101 MHz, DMSO-d_6) δ 168.78 (2C),

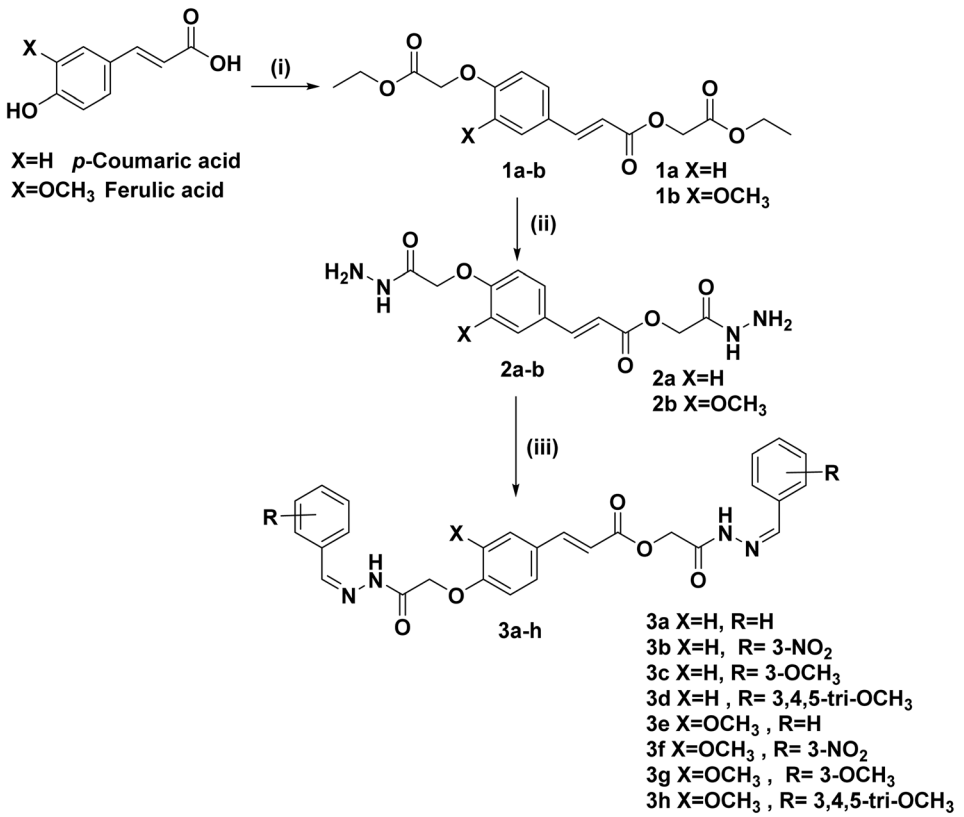

Reagents and conditions: (i) Ethyl 2-chloroacetate, dry DMF, anhydrous K_2CO_3, reflux 12h, **(ii)** Hydrazine hydrate, MeOH, reflux 9h, **(iii)** Aromatic aldehydes, MeOH, Glacial acetic acid, reflux 5h.

Scheme 1 Synthesis of compounds 2a–b & 3a–h.

166.92, 164.01 (2C), 159.54, 147.97, 144.27 (2C), 143.81 (2C), 130.00 (2C), 129.89 (2C), 126.85 (2C), 119.62, 116.36 (2C), 115.20 (2C), 115.11, 114.95 (2C), 66.44, 64.85, 55.15 (2C). Anal. calcd. for: $C_{29}H_{28}N_4O_7$: C, 63.96; H, 5.18; N, 10.29; O, 20.57. Found: C, 64.15; H, 5.29; N, 10.45.

3.1.4 2-Oxo-2-(2-((*E*)-3,4,5-trimethoxybenzylidene)hydrazinyl)ethyl (*E*)-3-(4-(2-oxo-2-(2-((*E*)-3,4,5-trimethoxybenzylidene) hydrazinyl)ethoxy)phenyl)acrylate (3d). Gray; yield 77%; M.p.; 186–188 °C; IR (cm^{-1}): 3242 (NH), 1694 (N=C), 1653 (C=O), 1248 (C–O–C). EI-MS (*m*/*z*, %): 664 (M^+); ^{1}H NMR (400 MHz, DMSO-d_6): δ 11.66 (s, 1H, N**H**), 8.26 (s, 1H, C**H**=N), 7.94 (s, 1H, C**H**=N), 7.72–7.66 (m, 2H, Ar–**H**), 7.62 (d, J = 16 Hz, 1H, C**H**=CH), 7.06–6.97 (m, 6H, Ar–**H**), 6.49 (d, J = 16 Hz, 1H, CH=C**H**), 5.24 (s, 2H, COO–**CH$_2$**), 4.75 (s, 1H, N**H**), 3.83 (s, 12H, 4× O**CH$_3$**), 3.72 (s, 6H, 2× O**CH$_3$**), 3.71 (s, 2H, O–**CH$_2$**); ^{13}C NMR (101 MHz, DMSO-d_6) δ 168.79 (2C), 166.94, 160.22, 153.17 (4C), 144.29 (2C), 144.16, 143.78 (2C), 130.12 (2C), 130.02 (2C), 126.83, 115.58, 114.95 (2C), 104.28 (4C), 66.42, 64.91, 60.13 (2C), 55.97 (4C). Anal. calcd. for: $C_{33}H_{36}N_4O_{11}$: C, 59.63; H, 5.46; N, 8.43; O, 26.48. Found: C, 59.80; H, 5.67; N, 8.69.

3.1.5 2-(2-((*E*)-Benzylidene)hydrazinyl)-2-oxoethyl(*E*)-3-(4-(2-(2-((*E*)-benzylidene)hydrazinyl)-2-oxoethoxy)-3-methoxyphenyl)acrylate (3e). Gray; yield 89%; M.p.; 108–110 °C; IR (cm^{-1}): 3217 (NH), 1635 (N=C), 1550 (C=O), 1229 (C–O–C). EI-MS (*m*/*z*, %): 514 (M^+); ^{1}H NMR (400 MHz, DMSO-d_6): δ 11.68 (s, 1H, N**H**), 8.31 (s, 1H, C**H**=N), 8.24 (s, 1H, C**H**=N), 8.07–7.71 (m, 4H, Ar–**H**), 7.60 (d, J = 16 Hz, 1H, C**H**=CH), 7.45–6.88 (m, 9H, Ar–**H**), 6.57 (d, J = 16 Hz, 1H, CH=C**H**), 5.21 (s, 2H, COO–**CH$_2$**), 4.71 (s, 1H, N**H**), 3.85 (s, 3H, O**CH$_3$**), 3.72 (s, 2H, O–**CH$_2$**). ^{13}C NMR (101 MHz, DMSO-d_6) δ 169.33 (2C), 167.54, 160.21, 148.64, 144.90, 144.58 (2C), 134.57 (2C), 130.82 (2C), 130.63 (4C), 129.41 (4C), 127.77, 127.57, 116.19, 115.82, 115.57, 67.06, 65.43, 51.93. Anal. calcd. for: $C_{28}H_{26}N_4O_6$: C, 65.36; H, 5.09; N, 10.89; O, 18.66. Found: C, 65.62; H, 5.19; N, 11.06.

3.1.6 2-(2-((*E*)-3-Nitrobenzylidene)hydrazinyl)-2-oxoethyl(-*E*)-3-(3-methoxy-4-(2-(2-((*E*)-3-nitrobenzylidene)hydrazinyl)-2-oxoethoxy)phenyl)acrylate (3f). White; yield 86%; M.p.; 154–156 °C; IR (cm^{-1}): 3260 (NH), 1686 (N=C), 1666 (C=O), 1552 (NO_2 Asym), 1335 (NO_2 Sym), 1249 (C–O–C). EI-MS (*m*/*z*, %): 604 (M^+); ^{1}H NMR (400 MHz, DMSO-d_6): δ 11.86 (s, 1H, N**H**), 8.50 (s, 1H, C**H**=N), 8.42 (s, 1H, C**H**=N), 8.26–8.12 (m, 4H, Ar–**H**), 7.75–7.71 (m, 2H, Ar–**H**), 7.59 (d, J = 16 Hz, 1H, C**H**=CH), 7.41–6.89 (m, 5H, Ar–**H**), 6.56 (d, J = 16 Hz, 1H, CH=C**H**), 5.26 (s, 2H, COO–**CH$_2$**), 4.75 (s, 1H, N**H**), 3.85 (s, 3H, O**CH$_3$**), 3.71 (s, 2H, O–**CH$_2$**); ^{13}C NMR (101 MHz, DMSO-d_6) δ 169.13 (2C), 164.63, 149.92, 149.15, 148.35 (2C), 145.64, 144.76 (2C), 141.86 (2C), 133.03 (2C), 130.50 (2C), 128.12, 127.34 (2C), 124.31, 122.63 (2C), 116.04, 111.21, 111.09, 67.23, 65.25, 55.83. Anal. calcd. for $C_{28}H_{24}N_6O_{10}$: C, 55.63; H, 4.00; N, 13.90; O, 26.47. Found: C, 55.49; H, 4.13; N, 14.15.

3.1.7 2-(2-((*E*)-3-Methoxybenzylidene)hydrazinyl)-2-oxoethyl (*E*)-3-(3-methoxy-4-(2-(2-((*E*)-3-methoxybenzylidene) hydrazinyl)-2-oxoethoxy)phenyl)acrylate (3g). Yellowish white; yield 84%; M.p.; 102–104 °C; IR (cm^{-1}): 3322 (NH), 1677 (N=C), 1657 (C=O), 1259 (C–O–C). EI-MS (*m*/*z*, %): 574 (M^+); ^{1}H NMR (400 MHz, DMSO-d_6): δ 11.64 (s, 1H, N**H**), 8.27 (s, 1H, C**H**=N), 7.99 (s, 1H, C**H**=N), 7.60 (d, J = 16 Hz, 1H, C**H**=CH), 7.41–6.87 (m, 11H, Ar–**H**), 6.57 (d, J = 16 Hz, 1H, CH=C**H**), 5.22 (s, 2H, COO–**CH$_2$**), 4.72 (s, 1H, N**H**), 3.85 (s, 3H, O**CH$_3$**), 3.80 (s, 6H, 2× O**CH$_3$**), 3.72 (s, 2H, O–**CH$_2$**); ^{13}C NMR (101 MHz, DMSO-d_6) δ 168.76 (2C), 167.00, 159.55 (2C), 147.75, 144.69 (2C), 144.51, 143.77 (2C), 135.38, 129.94 (2C), 127.17, 120.09, 119.63 (2C), 115.92 (2C), 115.45, 111.63 (2C), 111.35, 111.00, 65.12, 64.53, 55.20 (2C), 51.36. Anal. calcd. for: $C_{30}H_{30}N_4O_8$: C, 62.71; H, 5.26; N, 9.75; O, 22.28. Found: C, 62.88; H, 5.41; N, 9.94.

3.1.8 2-Oxo-2-(2-((*E*)-3,4,5-trimethoxybenzylidene)hydrazinyl)ethyl(*E*)-3-(3-methoxy-4-(2-oxo-2-(2-((*E*)-3,4,5tri-methoxybenzylidene)hydrazinyl)ethoxy)phenyl) acrylate (3h). Reddish white; yield 79%; M.p.; 140–142 °C; IR (cm^{-1}): 3074 (NH), 1626 (N=C), 1603 (C=O), 1257 (C–O–C). EI-MS (*m*/*z*, %): 694 (M^+); ^{1}H NMR (400 MHz, DMSO-d_6): δ 11.65 (s, 1H, N**H**), 8.21 (s, 1H, C**H**=N), 7.94 (s, 1H, C**H**=N), 7.60 (d, J = 16 Hz, 1H, C**H**=CH), 7.42–6.86 (m, 7H, Ar–**H**), 6.57 (d, J = 16 Hz, 1H, CH=C**H**), 5.23 (s, 2H, COO–**CH$_2$**), 4.71 (s, 1H, N**H**), 3.87 (s, 3H, O**CH$_3$**), 3.82 (s, 12H, 4× O**CH$_3$**), 3.72 (s, 6H, 2× O**CH$_3$**), 3.70 (s, 2H, O–**CH$_2$**); ^{13}C NMR (101 MHz, DMSO-d_6) δ 169.49 (2C), 167.72, 153.88 (4C), 149.72, 148.61, 145.38 (2C), 145.21, 144.51 (2C), 130.21 (2C), 127.85, 123.21, 116.64, 111.91, 111.70, 104.97 (4C), 65.89, 60.86 (2C), 56.67 (5C), 56.46. Anal. calcd. for $C_{34}H_{38}N_4O_{12}$: C, 58.78; H, 5.51; N, 8.07; O, 27.64. Found: C, 59.05; H, 5.67; N, 8.26.

3.2 Biology assessment

3.2.1 Cytotoxicity against MCF-7, HepG2, A549 and normal WISH cells using MTT assay. MCF-7, HepG2, A549, and normal (WISH) cells were purchased from the National Research Institute, Egypt, and cultured in "RPMI-1640 medium L-Glutamine (Lonza Verviers SPRL, Belgium, cat#12-604F)". All cells were incubated at 37 °C in a 5% carbon dioxide atmosphere (NuAire). A plate of 96 wells was used, and cells were seeded in triplicate at a density of 5×10^4 cells. Compounds with doses of 6.25, 12, 25, 50, and 100 μM were added to the cells on the second day.[43]

3.2.2 EGFR and VEGFR-2 kinase inhibition assays. All molecules were evaluated for their EGFR (BPS Bioscience Corporation Catalog #40321) and VEGFR-2 kinase inhibition using (BPS Bioscience Corporation catalog#40325) using ELISA kit (Enzyme-Linked Immunosorbent Assay). They were solved in DMSO (0.1%), and five serial dilutions were set following the manufacturer's instructions.[44,45]

3.2.3 Investigation of apoptosis

3.2.3.1 Annexin V/PI staining and cell cycle analysis. MCF-7 cells were seeded into 6-well culture plates (3–5× 10^5 cells per well) and incubated overnight. For 48 hours, cells were exposed to **3f** and **3h** at IC_{50} values. After that, the cells and medium supernatants were washed with ice-cold water. PBS. Then, the cells were suspended in 100 μL of annexin binding buffer solution "25 mM $CaCl_2$, 1.4 M NaCl, and 0.1 M Hepes/NaOH, pH 7.4" and incubated with "Annexin V-FITC solution (1 : 100) and propidium iodide (PI)" at a concentration equals 10 μg mL^{-1} in the dark for 30 min. Furthermore, the stained cells were collected using a BD FACSCalibur™ Flow Cytometer.[46–48]

3.2.3.2 Real-time-polymerase chain reaction for the selected genes. To probe the apoptotic pathway further, the expression of Bcl-2, an anti-apoptotic gene, and the pro-apoptotic genes "P53, Bax, and Caspapses-3,8,9" were studied. MCF-7 cells were then treated with compound **3f** at their IC_{50} values for 48 h. After treatment, the RT-PCR reaction was carried out following routine work.[49,50]

3.2.4 *In vivo* study. The experimental animals were randomly divided into four groups. Group 1 served as the normal saline control. Group 2 served as the SEC control (1×10^6 cells per mouse). Group 3 served as the compound **3f**-treated group (6 mg per kg B. Wt., I.P.). Group 4 received the standard anticancer drug of Sorafenib (6 mg per kg B. Wt., I.P.). Body weight and survival were recorded daily until the 24th day in both treated and control groups. At the end of the experiment, the anesthetized animals were then sacrificed for the examination of the antitumor activity, histopathological and immunohistochemical examination. The detailed methodology of tumor inoculation, treatments, histopathological of tumor tissues and immunohistochemical investigations of anti-BCL-2 (clone 124, 1 : 100, CST), anti-cleaved caspase-3 (Asp175, 1 : 100, CST), and anti-EGFR (clone 31G7, 1 : 50, Thermo Fisher) were performed according to the reported procedure,[51–53] as described in the SI. The experimental protocol was supported in the supplementary, and it was approved by Suez Canal University, Egypt, Faculty of Pharmacy's Ethical Committee which granted clearance for all study procedures (202206M3).

3.3 Molecular docking

The following codes were used to derive the atomic coordinates of kinase biotargets from RCSB_PDB: in accordance with the previous research, the AutoDock software v1.2.0 was employed to prepare and minimize VEGFR-2: 4asd[54] and EGFR: 4hjO[55] under AMBER/partial charges modified forcefields. The binding site was delineated to accommodate the co-crystallized ligands. The docking grid box was configured with dimensions of $20 \times 20 \times 20$ Å^3 to include all the identified critical binding residues inside the kinase pockets. The molecular docking process was conducted using the AMBER Forcefield and a Lamarckian/Genetic Algorithm to create the poses of the examined ligands.[56]

The docking parameters were established to ensure 100 exhaustiveness, 20 iterated binding modes, and a maximum free-binding energy difference of 4 kcal mol^{-1} between the predicted binding modes.[57] The optimal projected posture was chosen based on elevated docking scores, a low root-mean-square deviation (RMSD) of less than 2.00 Å from the ligand, and/or shown interactions with critical pocket residues consistent with small molecule kinase inhibitors. PyMol v2.0 was used to display the molecular modeling results and examine compound-kinase interactions and conformations.

4 Discussion

4.1 Chemistry

The synthesis started with the alkylation of *p*-coumaric acid and ferulic acid using ethyl chloroacetate in DMF in the presence of anhydrous K_2CO_3 to afford the corresponding esters **1a–b**, respectively. The success of the reaction was confirmed through ^{1}HNMR spectra where the ester part appeared clearly as two sharp singlets at a range of δ 4.86–4.76 for four protons of two (CH_2–O), up-field quartet for four protons of two (CH_2) at range of δ 4.18–4.17, and up-field triplet for six protons of two (CH_3) at δ 1.22. Then, compounds **1a–b** were refluxed with hydrazine hydrate in methanol to afford 2-hydrazineyl-2-oxoethyl (*E*)-3-(4-(2-hydrazineyl-2-oxoethoxy)-3-substituted phenyl) acrylate **2a–b**. The structure of the synthesized compounds was confirmed by ^{1}H NMR spectra, where the spectra displayed the disappearance of the up-field signals corresponding to two (O–CH_2–CH_3) groups in addition to the appearance of singlet belonging to two protons of NH_2 at δ 4.35–4.34. The resulted hydrazide derivatives **2a–b** underwent condensation with different aromatic aldehydes in the presence of a catalytic amount of glacial acetic acid to obtain target compounds **3a–h**. The success of the condensation was confirmed by ^{1}H NMR spectra of the synthesized candidates; the protons of two (CH=N) appeared as two downfield singlets in the range of δ 8.52–7.94. The spectra also showed two sharp singlets corresponding to two (CH_2–O) at a range of δ 5.28–5.21 and 3.72–3.70 in addition to two doublets for two protons of (CH=CH) at range of δ 7.65–7.57 and 6.59–6.46. The ^{1}HNMR spectra of compounds **3e–h** showed sharp up-field singlet for three protons of (OCH_3) of ferulic acid at range of δ 3.87–3.85, while compounds **3c** and **3g** showed a sharp up-field singlet for their ($2\times$ OCH_3) at δ 3.80. In addition, the ^{1}HNMR spectra of compounds **3d** and **3h** showed up-field singlets for their ($6\times$ OCH_3) in range of δ 3.83–3.72. Finally, ^{13}C NMR spectra of compound **3c–3h** showed peaks for carbon of (OCH_3) resonating at range of δ 55.15–55.97.

4.2 Biological investigations

4.2.1 Cell viability determination by MTT assay. The MTT assay was utilized to assess cytotoxic activity against MCF-7,

Table 1 IC_{50} values of the cytotoxicity of tested compounds against MCF-7, HepG2, A549 cancer cells and WISH normal cells using the MTT assay[a]

	IC_{50} μM ± SD			
Code	MCF-7 breast	HepG2 liver	A549 lung	WISH normal
2b	ND	16.5 ± 0.3	34.50 ± 1.2	46.50 ± 1.2
2a	14.20 ± 0.3	21.40 ± 0.7	18.70 ± 0.3	39.80 ± 1.5
3a	15.90 ± 0.2	ND	ND	39.80 ± 1.4
3b	9.18 ± 0.2	10.40 ± 0.3	11.60 ± 0.2	44.60 ± 1.6
3c	25.10 ± 0.8	ND	25.40 ± 0.7	41.80 ± 1.7
3d	1.16 ± 0.05	21.30 ± 0.8	33.10 ± 1.4	≥50
3e	14.60 ± 0.3	27.60 ± 1.1	29.80 ± 0.8	≥50
3f	1.04 ± 0.2	12.13 ± 0.1	13.30 ± 0.3	≥50
3g	13.40 ± 0.3	9.80 ± 0.4	8.75 ± 0.1	≥50
3h	1.10 ± 0.05	12.70 ± 0.4	11.50 ± 0.2	≥50
Sorafenib	3.04 ± 0.1	2.93 ± 0.2	1.26 ± 0.3	≥50

[a] IC_{50} values were calculated using the dose–response curves in GraphPad prism. Values are expressed as mean ± SD of three independent trials.

HepG2, A549 cancer cell lines, as well as normal WISH cells. As seen in Table 1, compared to Sorafenib (IC_{50} = 3.04 μM), compounds **3f**, **3h**, and **3d** showed strong cytotoxicity against MCF-7 cells with IC_{50} values of 1.04 μM, 1.1 μM, and 1.16 μM, respectively. Also, compounds **3f**, **3h**, and **3d** showed potential cytotoxicity against HepG2 cancer cells, with IC_{50} values that ranged from 12.12 to 13.3 μM. In the meanwhile, they exhibited promising cytotoxicity against A549 cells with IC_{50} values ranging from (11.5–33.1 μM).

It is worth noting that the activity profiles of the synthesized compounds against breast cancer cells were much more prominent on the other investigated ones. Exploring the structure–activity relationships of the synthesized bis-hydrazone acrylate derivatives (**3a–h**) against the MCF-7 breast cancer cell line would provide great insights guiding future lead optimization and development (Fig. 3). Notably, the SAR analysis revealed a pronounced dependence of the compounds' activity on the position and nature of aromatic substituents at both the terminal benzylidene moieties and phenyl acrylate core. A clear observation was highlighted that varying the substituents on the benzylidene rings showed a consistent activity trend. The unsubstituted benzylidene analog **3a** exhibited moderate activity profile (IC_{50} = 15.9 ± 0.2 μM), while as introducing relevant electron-withdrawing nitro group at the *meta*-position as seen with compound **3b** was assigned with enhanced cytotoxic activity of an IC_{50} value of 9.18 ± 0.2 μM. The latter observation highlights that the electron-deficient aromatic system of the synthesized compounds would favor an efficient interaction with the biological target. Contrarily, the same *meta*-position was intolerant to the incorporation of an electron-donating group like the methoxy moiety at **3c** where marked reduction within activity was observed (IC_{50} = 25.10 ± 0.8 μM). This detrimental impact of electron-donating group could possibly reduce binding affinity or sub-optimal electronic distributions. On the other hand, the 3,4,5-trimethoxybenzylidene derivative (**3d**) depicted the highest activity profile among these drug members, reaching an IC_{50} of 1.16 ± 0.05 μM that even surpassed that of the reference control, Sorafenib (IC_{50} of 3.04 ± 0.1 μM). The depicted dramatic enhancement can be attributed to the synergistic impacts of several methoxy moieties that can enhance aromatic π–π stacking, hydrogen bond potentiality, and even lipophilic characteristics for facilitated stronger engagement with intracellular targets.

Shifting our sight towards the methoxy group substitutions upon the phenyl acrylate main skeleton, this has pinpointed relevant insights regarding the comparative activity profiles among compounds **3e–h**. Notably, comparative analysis between **3a** and **3e** highlighted only a marginal improvement with IC_{50} of just 14.6 μM for the earlier compound. The latter signifies a marginal influence for the methoxy substitution on the core ring, particularly when combined with an unsubstituted benzylidene scaffold. Nonetheless, a pronounced activity enhancement was observed upon combining the core ring substitution with electron-withdrawing group like nitro, on the benzylidene ring. This was obvious with compound **3f** harboring both the methoxy-substituted phenyl core and *meta*-nitro benzylidene unit, which demonstrated excellent potency of IC_{50} = 1.04 ± 0.2 μM. This compound represents the most active compound within the entire synthesized series. The later SAR observation suggests a synergistic electronic effect of both the methoxy group and strong electron-withdrawing substituent towards an enhanced molecular orientation and/or target engagement. Similar activity fashion was also depicted with methoxy-harboring benzylidene analogs, like compound **3g** possessing moderate activity (IC_{50} = 13.40 ± 0.3 μM), while compound **3h** with triple methoxy benzylidene groups showed a restored high potency (IC_{50} = 1.10 ± 0.05 μM) in being comparable to **3d** (IC_{50} = 1.16 ± 0.05 μM), yet superior to Sorafenib.

4.2.2 EGFR, VEGFR2 dual kinase inhibition enzymatic assay. To identify their molecular targets, compounds **3f**, **3h**,

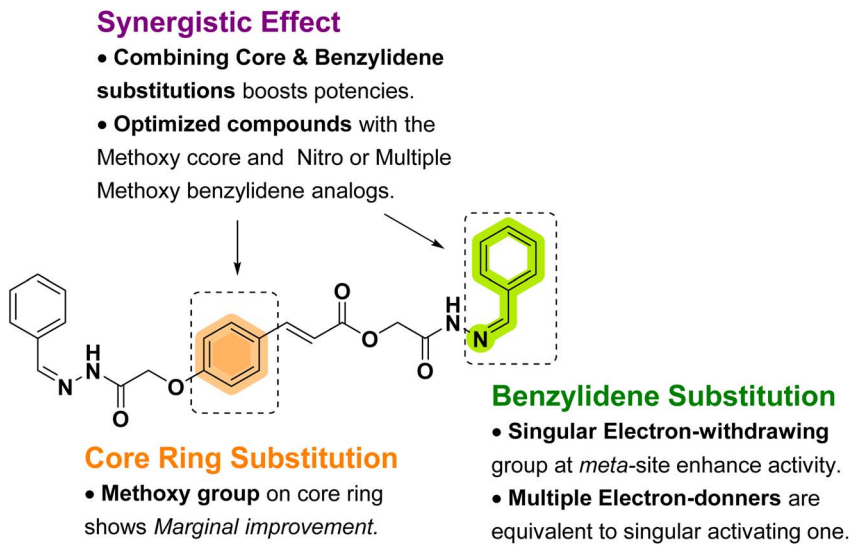

Fig. 3 SAR analysis of the synthesized bis-hydrazone acrylate analogs regarding activity optimization.

and **3d** were evaluated for their inhibitory activities against EGFR/VEGFR2. As shown in Table 2, the drugs that were evaluated demonstrated encouraging action in inhibiting both the EGFR and VEGFR2 kinases; interestingly, as shown in Fig. 4, compound **3f** had a lower IC_{50} value (75.4 nM) and a higher rate of EGFR inhibition (90.4% *vs.* 85% with Sorafenib; IC_{50} = 69.8 nM). Comparing compound **3f** to Sorafenib, which inhibits VEGFR2 by 87.3% (IC_{50} = 36.2 nM), compound **3f** showed a significantly higher level of efficacy (IC_{50} = 32.4 nM).

4.2.3 Annexin V/PI staining with cell cycle analysis. Using flow cytometric measurement of Annexin V/PI staining, we investigated apoptotic cell death in both untreated and treated MCF-7 cells to examine the apoptotic effect of compounds **3f** and **3h** at their IC_{50} values. Fig. 5A demonstrated that compound **3f** significantly increased the apoptosis ratio of MCF-7 cells by 32.9% and compound **3h** by 29.73%, respectively, as compared to the untreated control, which had a death rate of 0.95%.

Following treatment with cytotoxic agents, DNA flow cytometry was used to ascertain the cell population in each cell phase. As seen in (Fig. 5B), treatment with compounds **3f** and **3h** considerably raised the G1-phase cell population by 79.6% and 84.3%, respectively, compared to the control group's 53.3%, although there was a decline in S and G2/M phase cells. The treatment of MCF-7 cells with compounds **3f** and **3h** resulted in cell death, halting their proliferation in the G1 phase.

4.2.4 Gene expression of apoptosis-related genes using the RT-PCR. By comparing the RT-PCR levels of the genes induced by apoptosis in treated and control cells of MCF-7, we were able to confirm that compound **3f** caused cell death in the MCF-7 cells, validating the apoptosis-inducing activity. As seen in (Fig. 6), compound **3f** upregulated P53 levels by 5.02-fold change, caspase-3,8,9 levels by 9.2, 2.7, and 7.2-fold change, Bax by 5.62-fold. At the same time, it inhibited the Bcl-2 as anti-apoptotic gene by 0.4-fold change. Consequently, the results demonstrated that compound **3f** treatment triggered apoptotic cell death *via* an intrinsic apoptotic mechanism.

4.3 *In vivo* studies

To validate the cytotoxic activity of **3f** towards SEC propagation, the SEC-bearing mice model was used, with different treated groups. According to the data shown in Fig. 7A, the mass of malignancy increased by 298 mg throughout the assessment period. A solid tumor mass of 132 mg and 116 mg, respectively, was achieved after treatment with compound **3f** and Sorafenib, demonstrating significant cytotoxic effects. The tumor volume consequently decreased from 319 mm^3 in the SEC-bearing model to 134 mm^3 and 119.6 mm^3, respectively. Results showed that both treatments effectively reduced tumor growth by 57.9% and 62.5%, respectively, suggesting that they were effective in inhibiting the proliferation of SECs, as shown in Fig. 7.

4.3.1 Histological examination of the solid ascites tissues. Histological analysis of solid Ehrlich carcinoma (SEC) cells from SEC group (Fig. 8a) samples revealed distinct characteristics across different treatment groups. The untreated ascites tissue, examined at 100× magnification, displayed dense cellular aggregates with sheet-like arrangements, characterized by dark purple-staining nuclei and pink fibrous strands with clear architectural organization. The solid ascites tissue from the ascites group, viewed at 400× magnification (Fig. 8b), exhibited marked cellular pleomorphism with prominent nucleoli, high nuclear-to-cytoplasmic ratios, and irregular nuclear membranes, showing significant cellular disorganization. In the compound of **3f**-treated group (400× magnification) (Fig. 8c), the solid ascites tissue demonstrated malignant cells arranged in linear patterns with pink fibrous stromal bands, nuclear atypia, visible mitotic figures, and darker chromatin patterns. Finally, the standard drug of Sorafenib group (Fig. 8d), examined at 200× magnification, demonstrated significant therapeutic improvements in tissue architecture and cellular characteristics. The histological analysis revealed a well-organized cellular pattern with better-differentiated cells and reduced cellular crowding. Notable features included a more balanced distribution of inflammatory cells throughout the tissue, along with enhanced stromal organization. The treatment appeared to promote a more defined tissue architecture, characterized by more uniform nuclear morphology and distinct cytoplasmic boundaries. These improvements in cellular morphology and tissue organization.

4.3.2 Immunohistochemical findings. Fig. 9a–c showed in the untreated SEC group, strong cytoplasmic BCL-2 immunoreactivity was detected in most of the tumor cells, with a high percentage area indicating marked anti-apoptotic activity. In the **3f**-treated group, BCL-2 expression was moderately reduced, with fewer positive cells and lower staining intensity compared to the untreated group. Sorafenib-treated tissues demonstrated a significant downregulation of BCL-2, with weak and patchy staining confined to scattered tumor cells, reflecting inhibition of survival signaling. Quantitative analysis revealed that BCL-2 expression was significantly reduced in the **3f** group compared to untreated controls ($p < 0.05$) and further reduced in Sorafenib-treated tissues ($p < 0.005$ *vs.* untreated).

Fig. 9d–f showed apoptotic marker caspase-3 was rarely detected in the untreated group, consistent with low baseline apoptosis in highly proliferative tumors. In contrast, **3f**-treated tissues exhibited an increased proportion of caspase-3–positive cells, indicating induction of apoptosis, although the distribution remained heterogeneous. Sorafenib treatment produced the most robust caspase-3 expression, with strong nuclear/cytoplasmic positivity in a larger fraction of tumor cells, confirming activation of apoptotic pathways. Caspase-3 positivity

Table 2 IC_{50} values of enzyme targeting of EGFR, VEGFR2 dual kinase inhibition

	IC_{50} [nM] ± SD	
Compound	EGFR	VEGFR2
3f	75.4 ± 2.9	36.2 ± 1.1
3h	73.4 ± 2.7	38.6 ± 1.3
3d	82.3 ± 2.9	45.2 ± 1.4
Sorafenib	69.8 ± 1.9	30.1 ± 1.5

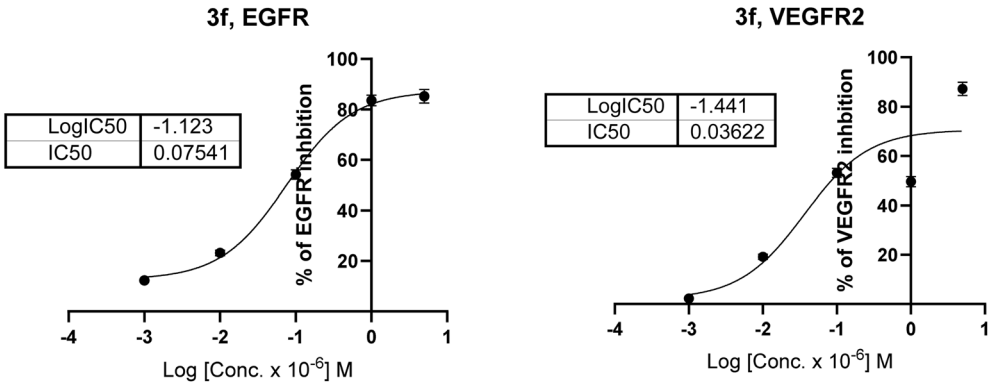

Fig. 4 Dose–response curves of the EGFR/VEGFR2 inhibition of compound **3f**. IC_{50} values were calculated using the non-linear regression dose–response curves in GraphPad prism. Values are expressed as mean ± SD of three independent trials.

showed the opposite trend, being lowest in untreated tumors and significantly elevated in **3f**-treated samples ($p < 0.05$), with the highest expression observed in the Sorafenib group.

Fig. 9g–i showed in the untreated SEC group strong membranous and cytoplasmic EGFR staining across most tumor cells, consistent with active growth signaling. In the **3f**-treated group, EGFR expression remained detectable but was reduced in both staining intensity and percentage of positive cells, suggesting partial inhibition of proliferative signaling. Sorafenib-treated tissues demonstrated markedly diminished EGFR immunoreactivity, with only faint residual membranous staining, reflecting effective suppression of receptor-mediated

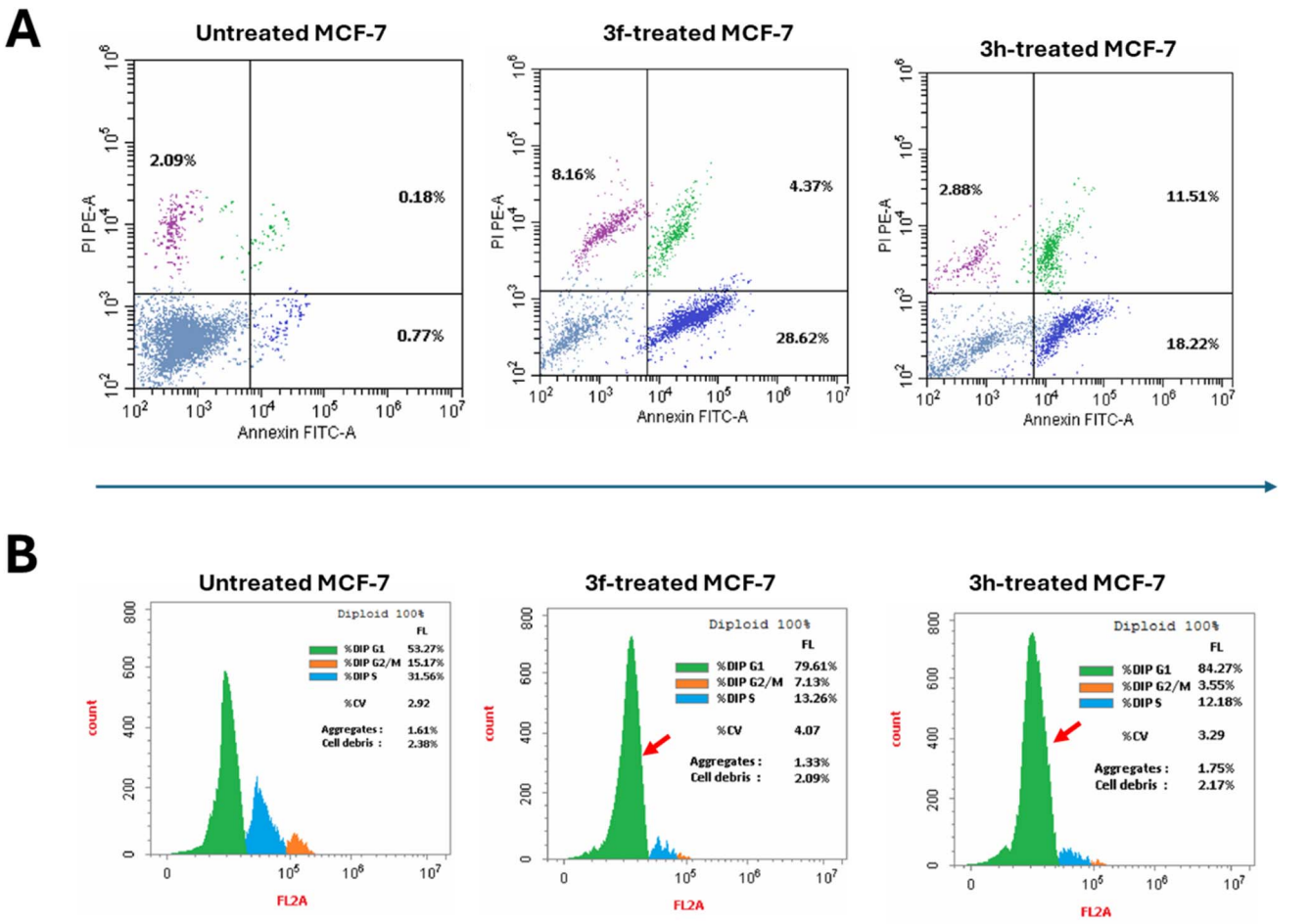

Fig. 5 (A) Cryptographs of Annexin-V/propidium iodide staining of untreated and **3f** and **3h**-treated MCF-7 cells with the IC_{50} for 48h. (B) Cell proportion (%) in each phase "G1, S, and G2/M" *via* flow cytometry of DNA content.

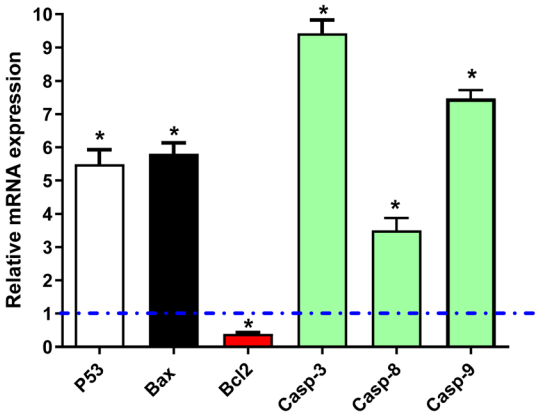

Fig. 6 Quantitative RT-PCR result analysis of the apoptosis-related genes P53, Bax, caspase-3, caspase-8, caspase-9, and Bcl-2, respectively, in untreated and treated MCF-7 cells with compound **3f** at the IC_{50} value for 48 h. "Values are expressed as mean ± SD of three independent trials. *($P \leq 0.05$) significantly different between **3f**-treated and SEC group using the unpaired *t*-test in GraphPad prism software".

proliferation. EGFR expression paralleled BCL-2, with the strongest expression in untreated SEC, moderate levels in **3f**, and the lowest in Sorafenib-treated tumors.

4.3.3 Histological and immunohistochemical analyses. The combined histological and immunohistochemical analyses of solid Ehrlich carcinoma (SEC) provided clear insights into how the tested treatments influenced tumor biology. In the untreated group, tumors displayed dense cellular aggregates, hyperchromatic nuclei, and sheet-like arrangements, all of which are typical features of a poorly differentiated and aggressive malignancy. These findings are consistent with earlier descriptions of SEC as a rapidly growing, undifferentiated neoplasm marked by high mitotic activity, nuclear pleomorphism, and stromal disruption.[58] On the immunohistochemical expression level, untreated tumors showed strong BCL-2 and EGFR expression with minimal caspase-3 activity, reflecting enhanced survival signaling and resistance to apoptosis.[59] This profile agrees with previous studies of,[60] and[61] showing that BCL-2 upregulation confers apoptosis resistance, while EGFR overexpression drives proliferation, angiogenesis, and invasion.

Treatment with the experimental compound **3f** preserved some malignant characteristics, including nuclear atypia and mitotic activity. However, it showed partial structural improvement, including linear tumor cell arrangements and fibrous stromal bands. Immunohistochemically, **3f** reduced BCL-2 and EGFR expression while moderately increasing cleaved caspase-3 activity. These changes suggest that **3f** interferes with tumor progression by dampening cell survival pathways and triggering apoptosis, though it does not fully normalize tumor architecture.[62] Similar outcomes have been reported for other natural and synthetic compounds tested in SEC, which reduced BCL-2 expression and increased caspase-3 activation but often left residual atypia, indicating partial or cytostatic effects rather than complete tumor regression.[63]

In contrast, Sorafenib treatment produced marked improvements both histologically and immunohistochemically. Tumors in this group exhibited better-organized architecture, reduced cellular crowding, more uniform nuclear features, and enhanced stromal organization. At the immunohistochemical expression level, Sorafenib strongly suppressed BCL-2 and EGFR expression while markedly increasing cleaved caspase-3 positivity. These results support the known mechanism of Sorafenib, which inhibits Raf/MEK/ERK and VEGFR signaling pathways, thereby exerting both anti-proliferative and anti-angiogenic effects.[64] The significant induction of caspase-3 observed in this study is consistent with previous work of[65] demonstrating that Sorafenib promotes apoptosis by blocking

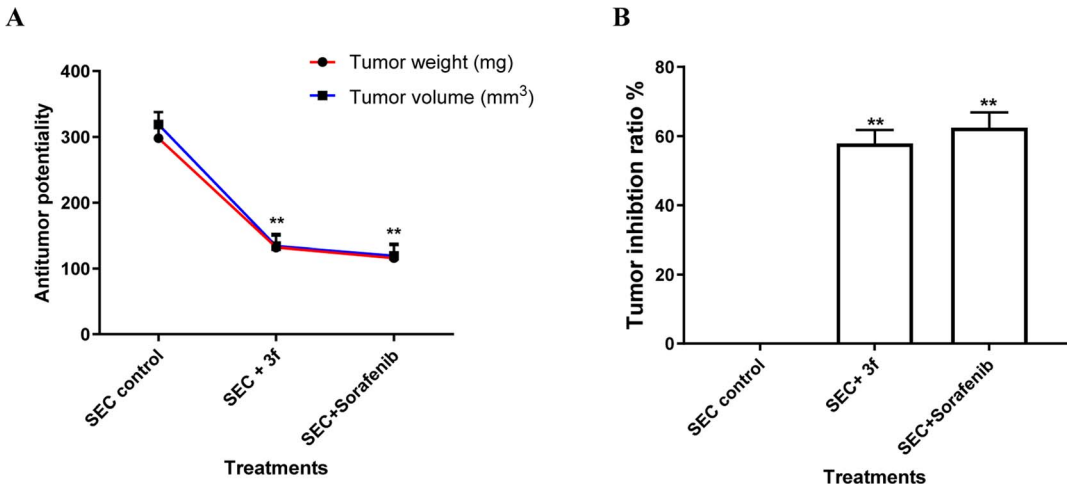

Fig. 7 Cytotoxicity of the compound **3f** in SEC-bearing mice model in different treated groups. (A) antitumor potentiality of compound **3f** using tumor volume and tumor volume, while (B) tumor inhibition ratio (TIR%), TIR% = $C - T/C \times 100$. In both graphs, treatments were administrated intraperitoneal (IP) with 6 mg per kg B. Wt. for two weeks, day after day, values are expressed as the average of five four mice in each group *($P \leq 0.05$) significantly different between **3f**-treated and SEC group using the unpaired *t*-test in GraphPad prism software.

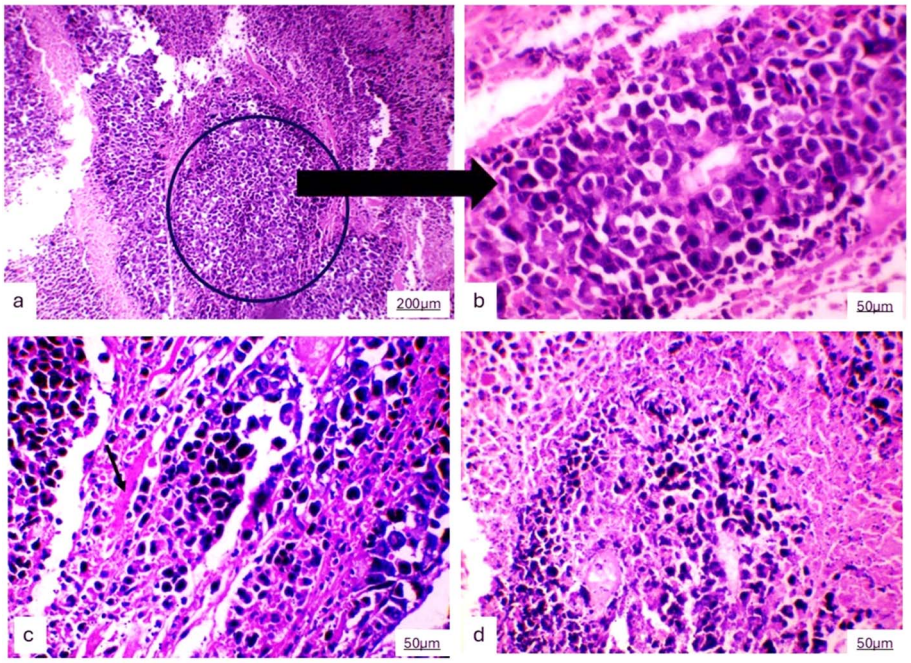

Fig. 8 Photomicrograph of the solid tumor tissue samples revealed distinct characteristics across different treatment groups. (a) The untreated ascites tissue, examined at 100× magnification, displayed dense cellular aggregates with sheet-like arrangements, characterized by dark purple-staining nuclei and pink fibrous strands with clear architectural organization. (b) The solid ascites tissue from the ascites group, viewed at 400× magnification, exhibited marked cellular pleomorphism with prominent nucleoli, high nuclear-to-cytoplasmic ratios, and irregular nuclear membranes, showing significant cellular disorganization. (c) In the compound **3f**-treated ascites group (400× magnification), the solid ascites tissue demonstrated malignant cells arranged in linear patterns with pink fibrous stromal bands (arrow), nuclear atypia, visible mitotic figures, and darker chromatin patterns. (d) The standard drug of Sorafenib revealed a well-organized cellular pattern with better-differentiated cells and reduced cellular crowding. Balanced distribution of inflammatory cells throughout the tissue, along with enhanced stromal organization.

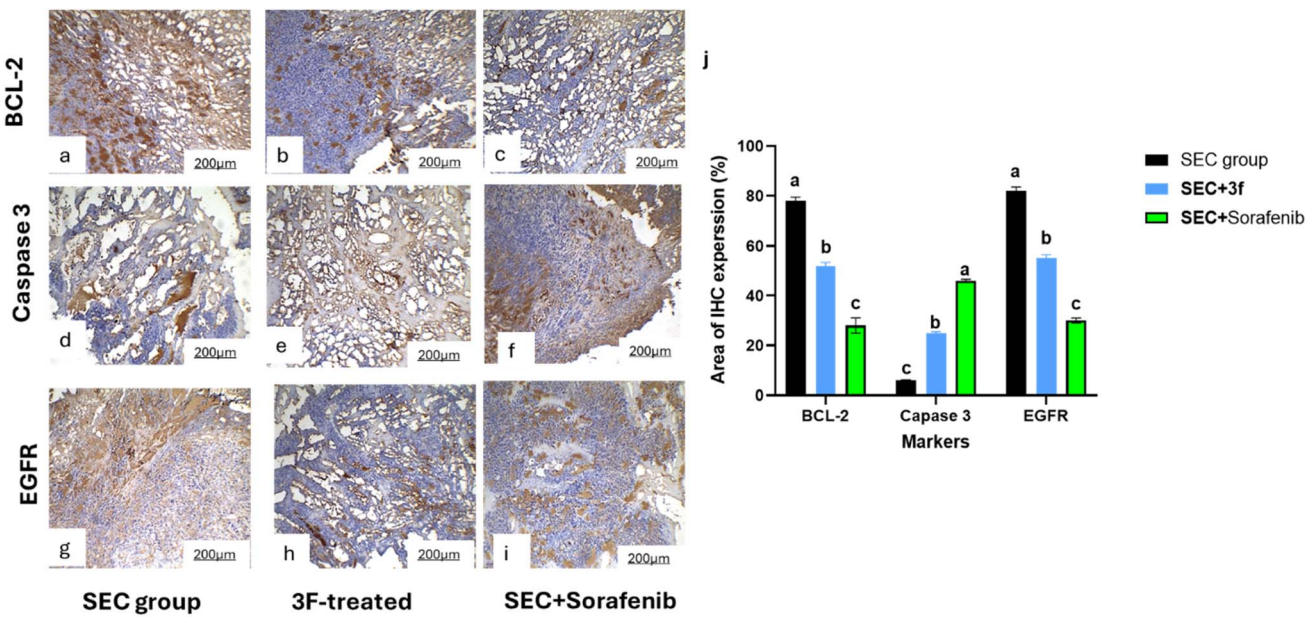

Fig. 9 Photomicrograph of the ascites tissue samples of the different groups revealed (a–c) the immunohistochemical expression of BCL-2, (d–f) the immunohistochemical expression of caspase 3 and (g–i) immunohistochemical expression of EGFR. (j) Bar chart expressed the means ± SD of the percentage positive area of BCL-2, caspase 3 and EGFR across untreated and treated groups. Different letters expressed significant difference $p < 0.05$ among groups. Anova test post hoc Tukey test.

pro-survival signaling and activating intrinsic apoptotic pathways.

Overall, these findings demonstrate that untreated SEC tissues maintain the classical profile of an aggressive tumor, while **3f** exerts partial inhibitory effects on tumor growth and apoptosis resistance. Sorafenib, on the other hand, produced robust therapeutic responses, restoring tissue organization and shifting the balance toward apoptosis. This highlights the value of BCL-2, caspase-3, and EGFR as reliable biomarkers of therapeutic efficacy in SEC. While **3f** showed a measurable activity, its effects are incomplete compared with Sorafenib, suggesting potential utility as an adjunct or in combination therapy.

4.4 Molecular modelling investigation

Molecular modeling studies are generally acknowledged as important in directing subsequent lead development and optimization efforts.[66] Thus, we adopted a highly validated molecular modeling technique to investigate the molecular characteristics of the binding affinity and pharmacodynamics of the synthesized compounds towards VEGFR-2 (PDB code: 4asd) and EGFR (PDB code: 4hjo). The docking scores obtained for **3f**, **3h**, and **3d** against EGFR indicated comparable binding profiles at ΔG scores −9.48, −8.79, and −8.38 kcal mol^{-1}, respectively, with **3f** exhibiting the quite higher binding affinity than the other analogs. Concerning the docking scores for the same compounds at the VEGFR2 pocket, the docking energies were depicted at −10.12, −9.37, and −9.33 kcal mol^{-1}, respectively, with a favored binding value for **3f**. Higher docking scores at VEGFR2 *versus* EGFR were in great agreement with the depicted *in vitro* enzymology findings, where compounds exhibited higher potency (lower IC_{50}s concentrations) at VEGFR2. The latter differential binding behavior could be related to the pocket's nature and size of each kinase enzyme as well as the predicted residue-wise binding patterns among the investigated compounds.

Typically, both EGFR and VEGFR2 endorse the classic ATP-binding sites that are often located inside the region between the enzyme's amino and carboxy lobes of the catalytic domains (Fig. 10).[67] The settlement of an ATP molecule inside the catalytic site is facilitated by a highly conserved Gly-rich loop (VEGFR-2 Gly841–Gly846; EGFR Gly719–Gly724) that aligns over the ATP pocket. Additional significant functional motifs are the activation β-loop (VEGFR-2 Asp1046–Glu1075; EGFR Asp855–Glu884), which contains the residues essential for the control of kinase activity and conformation. A shorter β-loop serves as the catalytic secondary structure (VEGFR-2 His1026–Asn1033; EGFR His835–Asn842), which supports the hydrophilic residues critical for the enzyme's transphosphorylation.[68,69] The interaction with the well-known motif (DFG) in the activation loop is linked to potent kinase inhibitors, since this pattern governs the enzyme's conformational transition between active and inactive states.

Despite comparable topology and important secondary structures, the pocket size of VEGFR2 is much more elongated than that of the EGFR enzyme.[39] Most of the reported VEGFR2 small molecule inhibitors generally adopt an elongated conformation for extended fitting towards the hydrophobic back cleft behind the gatekeeper residue, Thr916. On the contrary, a quite small and non-linear architecture (flatter) is the common feature of the EGFR inhibitors for fitting at the more compact and polar environment, particularly at the hinge and solvent-exposed pockets where residues such as Lys745, Asp855, and Thr790 contribute to more mixed hydrophobic-polar interactions.[70] This was clearly obvious with the differential architecture of the co-crystalline inhibitors of the kinase enzymes, Sorafenib (VEGFR2) and Erlotinib (EGFR) (Fig. 10). This could partially explain why our docked compounds with their elongated architecture managed to predict a higher docking score at VEGFR2 as compared to EGFR. On the other hand, the EGFR's pocket nature at the entrance could be more tolerant towards the polar substituents, that could explain why **3f** with its ionizable polar nitro groups, managed to depict higher docking energy at EGFR.

Comparative residue-wise interaction for the docked compounds at VEGFR2 highlighted quite comparable patterns with consistent interactions towards Cys919 (hinge region) and Glu885 residues. However, compound **3f** predicted more extended polar network towards the sidechain of Lys838, Pro839, Glu885, and Ile1044 as well as the mainchain of Asp1046 at the DFG motif (Fig. 10). The compound **3f** made the advent of polar terminal substitution, NO_2, to mediate relevant polar contacts at the entrance of the VEFR2 pocket. This could further add to the preferentially higher docking scores of **3f** as compared to the other congers, where fewer polar contacts were predicted. Moving towards the EGFR's binding site, the extended compounds were more occluding the enzyme's pocket rather than accommodating it. The extended structure of the compounds causes them to depict a more non-linear conformation at the EGFR's pocket. Compound **3f** *via* its more polar substituents (NO_2) managed to exhibit more extended polar contacts with EGFR's key residues including Met769 (hinge region), Ser696 (glycine-rich loop), and Glu738. Notably, all other derivatives managed to achieve a relevant contact towards the EGFR's hinge region residue, Met769, which has been reported as a crucial anchoring site for potent EGFR inhibitors.[71] Collective docking findings showed successful translation of the depicted enzyme inhibition assays at the previous biology investigation section, where compounds-VEGFR2 were of higher docking and IC_{50} values. The latter validates the docking findings.

Notably, the above-described docking findings provided great explanation of how these compounds exhibit dual inhibitory activity toward EGFR and VEGFR2 down to the molecular level of target-compound interaction patterns at the catalytic pockets. Molecular docking simulations highlighted the following structural features to be responsible for this dual-target activity; (i) the hydrazide–hydrazone moiety provides essential polar capabilities, acting as both hydrogen bond donors and acceptors to serve as relevant Hinge-region binding moieties. Molecular docking confirms these moieties engage with critical kinase amino acids within the hinge side, including EGFR Met769 and VEGFR2 Cys919; (ii) featuring a central aromatic scaffold derived from the parent phenolic

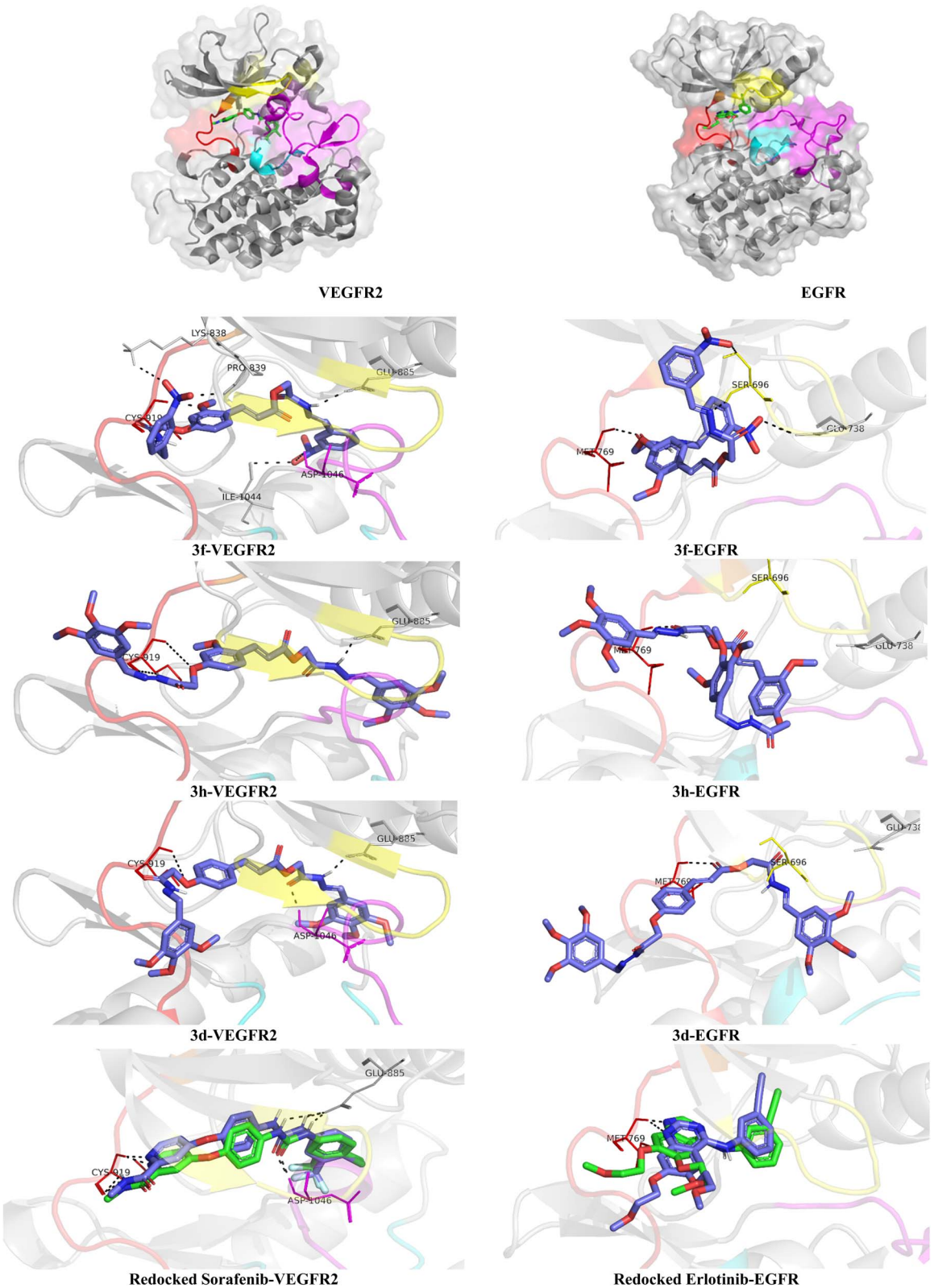

Fig. 10 Docking findings of the top-active synthesized compounds on dual kinase enzymes. Cartoon-surface 3D representation of the kinase highlighting the color-coded secondary structures; (yellow) Gly-rich loop, (red) hinge site, (magenta) activation loop, (cyan) catalytic motif, and (orange) gatekeeper residue; predicted binding modes of the **3f**, **3h**, and **3d** compounds (blue sticks) with the redocked co-crystallized for docking protocol validation aligned co-crystallized as green sticks over the redocked blue sticked poses of EGFR's reversible inhibitor, Erlotinib (PDB ID: 4hjo) and VEGFR-2's potent reversible inhibitor, Sorafenib (PDB ID: 4asd). Only key residues of binding at a 4 Å radius around the ligand are shown as lines and polar contacts as black-dash lines.

acids, allowed the compounds to mediate predicted hydrophobic contacts within the both kinases' central sub-pockets; (iii) harboring a second hydrazide–hydrazone moiety within the synthesized compounds' architecture, strategically positioned on the opposite side of the molecule, allowed them to promote polar contacts with the kinases' DFG-motif. Molecular interaction with this motif is crucial as it governs both enzymes' conformational transition (active/inactive states); (iv) docking simulation highlighted the important role of the terminal aromatic rings to satisfy the requirement for the kinases' double hydrophobic sub-pockets located on both sides of the ATP-adenine binding pocket; (v) the elongated structure of the synthesized compounds has been highlighted to be particularly well-suited for VEGFR2 pocket, which is more elongated than EGFR. This allows the compounds to fit into the hydrophobic back cleft behind the gatekeeper residue (Thr916); (vi) finally, specific substitution such as the electron-withdrawing nitro groups on the terminal rings (*e.g.*, compound **3f**), were reasoned to enhance activity. These polar groups predicted a more extended polar network contacting EGFR's Ser696 at Gly-rich loop and VEGFR2's Asp1046 at DFG motif.

The docking process was further validated by redocking the co-crystallized positive controls. The latter technique was used to ensure that the docking procedure and algorithm could predict a binding mode closely aligned in orientation and conformation with the co-crystallized or initial docking pose. The redocking of Erlotinib or Sorafenib at the ATP-binding sites of EGFR or VEGFR2, respectively, demonstrated significant superimposition between the redocked and co-crystallized/initial states, with RMSDs of 1.66 Å for EGFR and 1.04 Å for VEGFR2. Achieving low RMSDs below 2 Å is widely recognized as crucial for validating the used docking methodology in predicting binding modes and, therefore, binding energies with possible bioactivity relevance.[72,73] Consequently, it has been highlighted that redocked controls have effectively reproduced their crystalline ligand–target interaction patterns *via* polar contacts with critical residues, including those in the hinge region, DFG-activation loop, and/or deep hydrophobic pocket. Binding energy of redocked controls were at high negative energies; -10.79 kcal mol^{-1} for Sorafenib at VEGFR2 and -10.52 kcal mol^{-1} for Erlotinib at EGFR correlated to the found and reported inhibitory patterns of these reference agents.

4.5 Pharmacokinetic and physicochemical properties

Properties of our lead compound, **3f**, were evaluated in terms of predicted physiochemical properties, drug-likeness, and safety profile using the free on-line server ProTox3 (https://tox.charite.de/protox3/). Predicted physiochemical profiles showed moderate solubility and lipophilicity indices ($\log S = -5.14$ and $\log P = 1.94$), the thing that would confer a moderate oral bioavailability score and minimal CNS effect (limited blood–brain-barrier permeation). Owing to its large size (M. wt. > 500 g mol^{-1}) and excessive flexibility (>10), compound **3f** is not quite aligned with drug-likeness parameters. On the other hand, compound **3f** predicted a relevant safety profile since lacking any PAINS (pan-assay interference compounds) alerts, beside inactivity across various nuclear receptor signaling and stress response pathways. The compound further lacked any predictive binding affinity towards a wide-range of toxicity-related biotargets including adenosine receptor A2a (AA2AR), beta-2 adrenergic receptor (ADRB2), androgen receptor (ANDR), amine oxidase [flavin-containing] A (AOFA), corticotropin-releasing factor receptor 1 (CRFR1), D3 dopamine receptor (DRD3), estrogen receptors (ESR1/2), glucocorticoid receptor (GCR), histamine H1 receptor (HRH1), nuclear receptor subfamily 1 group I member 2 (NR1|2), kappa-type opioid receptor (OPRK), mu-type opioid receptor (OPRM), 3′,5′-cyclic-AMP phosphodiesterase 4D (PDE4D), prostaglandin G/H synthase 1 (PGH1), and progesterone receptor (PRGR). Additionally, compound **3f** predicted inactivity across several microsomal CYP enzymes (CYP1A2, CYP2C19, CYP2D6, CYP3A4, and CYP2E1), yet low prediction value for potential drug–drug interaction through CYP2C9. All above data suggest its potential enrollment within future lead optimization and development stage for prospective and comprehensive pre-clinical and clinical testing.

5 Conclusion

Considering the significant results of previous studies, which showed that FA and *P*-CA acid have strong anticancer effects due to their ability to inhibit EGFR and VEGFR2, new compounds were designed based on the structure of these nature-based building blocks. Among the synthesized analogs, compound **3f** was found to be the most potent in the series, exhibiting potent dual EGFR/VEGFR2 in relation to the standard kinase inhibitor, Sorafenib. The compound highlighted preferential apoptosis induction within the breast MCF-7 cells with a preferential target for increased G1-phase and decreased S-G2/M cell populations in MCF-7 cells. Following treatment at SEC-bearing cancer animal model, compound **3f** showed significant tumor mass reduction, inhibited proliferation, and a high efficacy and safety profile throughout histological analysis. The lead compounds further predicted a high safety profile with limited affinity towards several off-target macromolecules. However, challenging physiochemical properties, including solubility and high flexibility indices would hamper the compound's bioavailability and membrane permeation. This would prospect future structure optimization through restricted rotation as well as introduction of balanced polar/hydrophobic groups like triazole ring for improving bioavailability and membrane permeation indices. Additionally, prospect nano formulation of this lead compound can be proceeded for improving the compound's kinetics and enabled targeted delivery. Taken together, these findings support compound **3f** as a promising dual-target anticancer scaffold that merits further structural optimization to overcome its physicochemical limitations and advance its preclinical/clinical therapeutic potential for developing a next-generation anticancer agent.

Ethical statement

The Suez Canal University, Egypt, Faculty of Pharmacy's Ethical Committee has granted clearance for all study procedures (202206M3).

Author contributions

This work was carried out in collaboration among all authors. Authors designed the study, wrote the protocol, managed the analysis of the study, performed the statistical analysis, wrote the first draft of the manuscript, and managed the literature searches. All authors read and approved the final manuscript.

Conflicts of interest

The authors declare no conflict of interest.

Data availability

The data supporting this article, including ^{1}H NMR, ^{13}C NMR, and mass spectra of the synthesized compounds have been included as part of the supplementary information (SI) with the dose–response viability curves. Supplementary information is available. See DOI: https://doi.org/10.1039/d6ra01213b.

References

1 A. Najmi, *et al.*, Modern Approaches in the Discovery and Development of Plant-Based Natural Products and Their Analogues as Potential Therapeutic Agents, *Molecules*, 2022, **27**(2), 349.
2 M. J. Balunas and A. D. Kinghorn, Drug discovery from medicinal plants, *Life Sci.*, 2005, **78**(5), 431–441.
3 C. Drahl, B. F. Cravatt and E. J. Sorensen, Protein-reactive natural products, *Angew Chem. Int. Ed. Engl.*, 2005, **44**(36), 5788–5809.
4 D. J. Newman, G. M. Cragg and K. M. Snader, The influence of natural products upon drug discovery, *Nat. Prod. Rep.*, 2000, **17**(3), 215–234.
5 L. R. Ferguson, S. T. Zhu and P. J. Harris, Antioxidant and antigenotoxic effects of plant cell wall hydroxycinnamic acids in cultured HT-29 cells, *Mol. Nutr. Food Res.*, 2005, **49**(6), 585–593.
6 L. Y. Zang, *et al.*, Effect of antioxidant protection by p-coumaric acid on low-density lipoprotein cholesterol oxidation, *Am. J. Physiol.: Cell Physiol.*, 2000, **279**(4), C954–C960.
7 K. Pei, *et al.*, p-Coumaric acid and its conjugates: dietary sources, pharmacokinetic properties and biological activities, *J. Sci. Food Agric.*, 2016, **96**(9), 2952–2962.
8 S. Mozaffari Godarzi, *et al.*, Antioxidant effect of p-coumaric acid on interleukin 1-beta and tumor necrosis factor-alpha in rats with renal ischemic reperfusion, *Nefrologia*, 2020, **40**(3), 311–319.
9 Y. Zhao, *et al.*, Anti-inflammatory effects of p-coumaric acid in LPS-stimulated RAW264. 7 cells: Involvement of NF-κB and MAPKs pathways, *Med. Chem.*, 2016, **6**, 327–330.
10 F. Firdaus, *et al.*, Phenethyl p-coumarate and N-phenethyl-p-coumaramide: Synthesis, Characterization, Docking Studies, and Anticancer Activity through P388 Cell, *Sains Malays.*, 2022, **51**(4), 1085–1097.
11 J. I. Carmo-Martins, *et al.*, Esterification of p-Coumaric Acid Improves the Control over Melanoma Cell Growth, *Biomedicines*, 2023, **11**(1), 196.
12 S. Saremi, *et al.*, Induction of apoptosis and suppression of Ras gene expression in MCF human breast cancer cells, *J. Cancer Res. Ther.*, 2022, **18**(4), 1052–1060.
13 T. Burhanoğlu, *et al.*, Evaluation of the anticancer effects of hydroxycinnamic acid isomers on breast cancer stem cells, *Med. Oncol.*, 2025, **42**(3), 73.
14 D. M. Rodrigues, *et al.*, Novel synthetic derivatives of cinnamic and p-coumaric acids with anti-proliferative effect on breast MCF-7 tumor cells, *Nat. Prod. Res.*, 2023, **37**(24), 4210–4220.
15 X. Bao, *et al.*, Molecular mechanism of ferulic acid and its derivatives in tumor progression, *Pharmacol. Rep.*, 2023, **75**(4), 891–906.
16 T. Akihisa, *et al.*, Triterpene alcohol and sterol ferulates from rice bran and their anti-inflammatory effects, *J. Agric. Food Chem.*, 2000, **48**(6), 2313–2319.
17 E. Graf, Antioxidant potential of ferulic acid, *Free Radical Biol. Med.*, 1992, **13**(4), 435–448.
18 B. Janicke, *et al.*, The anti-proliferative effect of dietary fiber phenolic compounds ferulic acid and p-coumaric acid on the cell cycle of Caco-2 cells, *Nutr. Cancer*, 2011, **63**(4), 611–622.
19 W. Li, *et al.*, Biological activity evaluation and structure-activity relationships analysis of ferulic acid and caffeic acid derivatives for anticancer, *Bioorg. Med. Chem. Lett.*, 2012, **22**(19), 6085–6088.
20 R. Panwar, *et al.*, Characterization and anticancer potential of ferulic acid-loaded chitosan nanoparticles against ME-180 human cervical cancer cell lines, *Appl. Nanosci.*, 2016, **6**(6), 803–813.
21 S. R. O. Shajan, *et al.*, Folic acid-conjugated Ferulic acid-entangled Single-Walled Carbon Nanotubes: A targeted therapeutic approach for effective breast cancer treatment, *J. Drug Delivery Sci. Technol.*, 2025, **111**, 107111.
22 E. M. Johnson *et al.*, Anticancer, anti-inflammatory, and immune modulatory activity of ferulic acid fructo-oligosaccharide conjugated microparticle, *bioRxiv*, 2023, preprint, 2023.05.05.539559, DOI: 10.1101/2023.05.05.539559.
23 S. Ahmmed, *et al.*, Potential Therapeutic Efficacy of Ferulic Acid and Its Derivatives in the Management of Cancers: A Comprehensive Analysis With Mechanistic Insight, *Int. J. Food Sci.*, 2025, **2025**(1), 2256871.
24 R. Elrayess, *et al.*, 2-Phenylquinazolin-4(3H)-one scaffold as newly designed, synthesized VEGFR-2 allosteric inhibitors with potent cytotoxicity through apoptosis, *Arch. Pharm.*, 2023, **356**(6), e2200654.

25 R. Elrayess, *et al.*, Quinoline–hydrazone hybrids as dual mutant EGFR inhibitors with promising metallic nanoparticle loading: rationalized design, synthesis, biological investigation and computational studies, *New J. Chem.*, 2022, **46**(38), 18207–18232.
26 N. Ferrara, H. P. Gerber and J. LeCouter, The biology of VEGF and its receptors, *Nat. Med.*, 2003, **9**(6), 669–676.
27 C. King and K. Hristova, Direct measurements of VEGF-VEGFR2 binding affinities reveal the coupling between ligand binding and receptor dimerization, *J. Biol. Chem.*, 2019, **294**(23), 9064–9075.
28 M. Onda, *et al.*, Inhibition of VEGFR2 and EGFR signaling cooperatively suppresses the proliferation of oral squamous cell carcinoma, *Cancer Med.*, 2023, **12**(15), 16416–16430.
29 M. D. Paul and K. Hristova, Interactions between Ligand-Bound EGFR and VEGFR2, *J. Mol. Biol.*, 2021, **433**(13), 167006.
30 N. Roy, *et al.*, Plant Phenolics Ferulic Acid and P-Coumaric Acid Inhibit Colorectal Cancer Cell Proliferation through EGFR Down- Regulation, *Asian Pac. J. Cancer Prev.*, 2016, **17**(8), 4019–4023.
31 W. Tehami, *et al.*, New Insights Into the Anticancer Effects of p-Coumaric Acid: Focus on Colorectal Cancer, *Dose-Response*, 2023, **21**(1), 15593258221150704.
32 C. S. Kong, *et al.*, Antiangiogenic effects of p-coumaric acid in human endothelial cells, *Phytother. Res.*, 2013, **27**(3), 317–323.
33 M. Abotaleb, *et al.*, Therapeutic Potential of Plant Phenolic Acids in the Treatment of Cancer, *Biomolecules*, 2020, **10**(2), 221.
34 S. H. Son, *et al.*, Sustainable production of natural products using synthetic biology: Ginsenosides, *J. Ginseng Res.*, 2024, **48**(2), 140–148.
35 F. S. Albalawi, *et al.*, Purine-Hydrazone Scaffolds as Potential Dual EGFR/HER2 Inhibitors, *Pharmaceuticals*, 2025, **18**(7), 1051.
36 J. K. Nkoana, *et al.*, Examining the 2-aryl-5-nitrobenzofuran-based hydrazones for anti-breast (MCF-7) cancer activity, potential to induce cell cycle arrest and inhibit receptor tyrosine kinases (VEGFR-2 & EGFR), *Eur. J. Med. Chem.*, 2025, **298**, 118018.
37 M. I. Han, *et al.*, Design and synthesis of novel (S)-Naproxen hydrazide-hydrazones as potent VEGFR-2 inhibitors and their evaluation in vitro/in vivo breast cancer models, *Bioorg. Med. Chem.*, 2021, **37**, 116097.
38 A. G. Shtukenberg, *et al.*, Disrupting crystal growth through molecular recognition: designer therapies for kidney stone prevention, *J. Acc. Chem. Res.*, 2022, **55**(4), 516–525.
39 J. J. Liao and R. C. Andrews, Targeting protein multiple conformations: a structure-based strategy for kinase drug design, *Curr. Top. Med. Chem.*, 2007, **7**(14), 1394–1407.
40 N. Manju, *et al.*, Ethyl (naphthalen-2-yloxy)acetate, *IUCrData*, 2016, **1**(10), x161594.
41 S. Kumar, P. Kumar and N. Sati, Synthesis and biological evaluation of Schiff bases and azetidinones of 1-naphthol, *J. Pharm. BioAllied Sci.*, 2012, **4**(3), 246.
42 R. Elrayess, *et al.*, Synthesis and Antimicrobial Activities of Some Novel Benzimidazole and Benzotriazole Derivatives containing β-Lactam Moiety, *Life Sci. J.*, 2020, **10**, 1784–1793.
43 T. Mosmann, Rapid colorimetric assay for cellular growth and survival: application to proliferation and cytotoxicity assays, *J. Immunol. Methods*, 1983, **65**(1–2), 55–63.
44 M. S. Nafie, *et al.*, Quinoline-based thiazolidinone derivatives as potent cytotoxic and apoptosis-inducing agents through EGFR inhibition, *Chem. Biol. Drug Des.*, 2022, **99**(4), 547–560.
45 M. S. Nafie, M. A. Ali and M. M. Youssef, N-allyl quinoxaline derivative exhibited potent and selective cytotoxicity through EGFR/VEGFR-mediated apoptosis: In vitro and in vivo studies, *J. Biochem. Mol. Toxicol.*, 2024, **38**(4), e23690.
46 E. E. Eltamany, *et al.*, Comparative Assessment of the Antioxidant and Anticancer Activities of Plicosepalus acacia and Plicosepalus curviflorus: Metabolomic Profiling and In Silico Studies, *Antioxidants*, 2022, **11**(7), 1249.
47 F. M. Thabet, *et al.*, Design and synthesis of new bis(1,2,4-triazolo[3,4-b][1,3,4]thiadiazines) and bis((quinoxalin-2-yl) phenoxy)alkanes as anti-breast cancer agents through dual PARP-1 and EGFR targets inhibition, *RSC Adv.*, 2022, **12**(36), 23644–23660.
48 M. S. Goda, *et al.*, In Vitro and In Vivo Studies of Anti-Lung Cancer Activity of Artemesia judaica L. Crude Extract Combined with LC-MS/MS Metabolic Profiling, Docking Simulation and HPLC-DAD Quantification, *Antioxidants*, 2021, **11**(1), 17.
49 M. S. Nafie, *et al.*, Triaryl dicationic DNA minor-groove binders with antioxidant activity display cytotoxicity and induce apoptosis in breast cancer, *Chem.-Biol. Interact.*, 2020, **324**, 109087.
50 M. S. Nafie, *et al.*, Control of ER-positive breast cancer by ERalpha expression inhibition, apoptosis induction, cell cycle arrest using semisynthetic isoeugenol derivatives, *Chem.-Biol. Interact.*, 2022, **351**, 109753.
51 A. S. Castanet, *et al.*, Discovery of PIM-1 kinase inhibitors based on the 2,5-disubstituted 1,3,4-oxadiazole scaffold against prostate cancer: Design, synthesis, in vitro and in vivo cytotoxicity investigation, *Eur. J. Med. Chem.*, 2023, **250**, 115220.
52 H. A. Elsebaie, *et al.*, Discovery of new 1,3-diphenylurea appended aryl pyridine derivatives as apoptosis inducers through c-MET and VEGFR-2 inhibition: design, synthesis, in vivo and in silico studies, *RSC Med. Chem.*, 2024, **15**(7), 2553–2569.
53 F. T. Frajacomo, *et al.*, Solid Ehrlich carcinoma reproduces functional and biological characteristics of cancer cachexia, *Life Sci.*, 2016, **162**, 47–53.
54 M. McTigue, *et al.*, Molecular conformations, interactions, and properties associated with drug efficiency and clinical performance among VEGFR TK inhibitors, *Proc. Natl. Acad. Sci. U. S. A.*, 2012, **109**(45), 18281–18289.
55 J. H. Park, *et al.*, Erlotinib binds both inactive and active conformations of the EGFR tyrosine kinase domain, *Biochem. J.*, 2012, **448**(3), 417–423.

56 J. Eberhardt, *et al.*, AutoDock Vina 1.2.0: New Docking Methods, Expanded Force Field, and Python Bindings, *J. Chem. Inf. Model.*, 2021, **61**(8), 3891–3898.
57 Q. Xue, *et al.*, Evaluation of the binding performance of flavonoids to estrogen receptor alpha by Autodock, Autodock Vina and Surflex-Dock, *Ecotoxicol. Environ. Saf.*, 2022, **233**, 113323.
58 A. A. Winder, *et al.*, Neoplasms of the abdominal wall, *J. Abdom. Trauma Peritoneum Retrop.*, 2022, **10**(1), 2.
59 B. Yang, *et al.*, A shift in the Bax/Bcl-2 balance may activate caspase-3 and modulate apoptosis in experimental glomerulonephritis, *J. Kidney Int.*, 2002, **62**(4), 1301–1313.
60 M. Alam, *et al.*, Bax/Bcl-2 cascade is regulated by the EGFR pathway: therapeutic targeting of non-small cell lung cancer, *J. Front. Oncol.*, 2022, **12**, 869672.
61 X. Liu, *et al.*, Wogonin inhibits the proliferation and invasion, and induces the apoptosis of HepG2 and Bel7402 HCC cells through NF-κB/Bcl-2, EGFR and EGFR downstream ERK/AKT signaling, *Int. J. Mol. Med.*, 2016, **38**(4), 1250–1256.
62 K. Yaacoub, *et al.*, Role of the tumor microenvironment in regulating apoptosis and cancer progression, *J. Cancer Lett.*, 2016, **378**(2), 150–159.
63 I. Iksen, *et al.*, Comprehensive review of Bcl-2 family proteins in cancer apoptosis: Therapeutic strategies and promising updates of natural bioactive compounds and small molecules, *J. Phytother. Res.*, 2024, **38**(5), 2249–2275.
64 S. M. Wilhelm, *et al.*, Preclinical overview of sorafenib, a multikinase inhibitor that targets both Raf and VEGF and PDGF receptor tyrosine kinase signaling, *J. Mol. Cancer Ther.*, 2008, **7**(10), 3129–3140.
65 M. Wei, *et al.*, The advantages and challenges of sorafenib combination therapy: Drug resistance, toxicity and future directions, *J. Oncol. Lett.*, 2025, **30**(5), 1–20.
66 S. Saikia and M. Bordoloi, Molecular Docking: Challenges, Advances and its Use in Drug Discovery Perspective, *Curr. Drug Targets*, 2019, **20**(5), 501–521.
67 K. Budipramana and F. Sangande, Structural and molecular insights from dual inhibitors of EGFR and VEGFR2 as a strategy to improve the efficacy of cancer therapy, *Chem. Biol. Drug Des.*, 2024, **103**(5), e14534.
68 E. Kovacs, *et al.*, A structural perspective on the regulation of the epidermal growth factor receptor, *Annu. Rev. Biochem.*, 2015, **84**, 739–764.
69 S. A. Park, *et al.*, Structure and function of vascular endothelial growth factor and its receptor system, *BMB Rep.*, 2018, **51**(2), 73–78.
70 X. Zhang, *et al.*, An allosteric mechanism for activation of the kinase domain of epidermal growth factor receptor, *Cell*, 2006, **125**(6), 1137–1149.
71 T. Amelia, *et al.*, Structural Insight and Development of EGFR Tyrosine Kinase Inhibitors, *Molecules*, 2022, **27**(3), 819.
72 M. Kontoyianni, L. M. McClellan and G. S. Sokol, Evaluation of docking performance: comparative data on docking algorithms, *J. Med. Chem.*, 2004, **47**(3), 558–565.
73 A. S. A. Yassen, *et al.*, Novel curcumin-based analogues as potential VEGFR2 inhibitors with promising metallic loading nanoparticles: synthesis, biological evaluation, and molecular modelling investigation, *RSC Med. Chem.*, 2024, **15**(12), 4039–4067.